

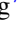



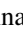





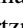
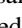

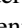

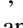


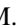


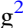




Multiwavelength Observations of the Blazar VER J0521+211 during an Elevated TeV Gamma-Ray State

C. B. Adams¹, P. Batista², W. Benbow³ , A. Brill⁴ , R. Brose⁵, J. H. Buckley⁶, M. Capasso⁷, J. L. Christiansen⁸, M. Errando⁶, Q. Feng⁷ , J. P. Finley⁹, G. M. Foote¹⁰, L. Fortson¹¹ , A. Furniss¹² , G. Gallagher¹³, A. Gent¹⁴ , C. Giuri², W. F. Hanlon³, D. Hanna¹⁵ , T. Hassan² , O. Hervet¹⁶ , J. Holder¹⁰, B. Hona¹⁷ , G. Hughes³, T. B. Humensky¹, W. Jin¹⁸ , P. Kaaret¹⁹ , M. Kertzman²⁰, D. Kieda¹⁷ , T. K. Kleiner², F. Krennrich²¹, S. Kumar¹⁵, M. J. Lang²² , M. Lundy¹⁵, G. Maier² , J. Millis²³, P. Moriarty²², R. Mukherjee⁷ , M. Nieves-Rosillo² , S. O'Brien¹⁵, R. A. Ong²⁴ , A. N. Otte¹⁴, S. Patel¹⁹, S. R. Patel², K. Pfrang² , M. Pohl⁵ , R. R. Prado², E. Pueschel² , J. Quinn²⁵, K. Ragan¹⁵ , P. T. Reynolds²⁶, D. Ribeiro¹ , E. Roache³, J. L. Ryan²⁴, I. Sadeh² , M. Santander¹⁸, G. H. Sembroski⁹, R. Shang²⁴, B. Stevenson²⁴, J. V. Tucci²⁷, V. V. Vassiliev²⁴, S. P. Wakely²⁸, A. Weinstein²¹, R. M. Wells²¹, D. A. Williams¹⁶, T. J. Williamson¹⁰

(The VERITAS Collaboration),

and

V. A. Acciari²⁹ , T. Aniello³⁰, S. Ansoldi^{31,32} , L. A. Antonelli³⁰ , A. Arbet Engels³³ , C. Arcaro³⁴, M. Artero³⁵ , K. Asano³⁶ , D. Baack³⁷ , A. Babić³⁸ , A. Baquero³⁹ , U. Barres de Almeida⁴⁰ , J. A. Barrio³⁹ , I. Batkovic³⁴ , J. Becerra González²⁹ , W. Bednarek⁴¹ , E. Bernardini³⁴ , M. Bernardos³⁴, A. Berti³³ , J. Besenrieder³³, W. Bhattacharyya⁴² , C. Bigongiari³⁰ , A. Biland⁴³ , O. Blanch³⁵ , H. Bökenkamp³⁷ , G. Bonnoli⁴⁴ , Ž. Bošnjak³⁸ , I. Burelli³¹, G. Busetto³⁴ , R. Carosi⁴⁵ , G. Ceribella³⁶ , M. Cerruti⁴⁶ , Y. Chai³³ , A. Chilingarian⁴⁷ , S. Cikota³⁸, E. Colombo²⁹ , J. L. Contreras³⁹ , J. Cortina⁴⁸ , S. Covino³⁰ , G. D'Amico⁴⁹ , V. D'Elia³⁰ , P. Da Vela^{45,50} , F. Dazzi³⁰ , A. De Angelis³⁴ , B. De Lotto³¹ , A. Del Popolo⁵¹ , M. Delfino^{35,52} , J. Delgado^{35,52} , C. Delgado Mendez⁴⁸ , D. Depaoli⁵³ , F. Di Piero⁵³ , L. Di Venere⁵⁴ , E. Do Souto Espiñeira³⁵ , D. Dominis Prester⁵⁵ , A. Donini³¹ , D. Dorner⁵⁶ , M. Doro³⁴ , D. Elsaesser³⁷ , V. Fallah Ramazani^{57,58} , L. Fariña³⁵ , A. Fattorini³⁷ , L. Font⁵⁹ , C. Fruck³³ , S. Fukami⁴³ , Y. Fukazawa⁶⁰ , R. J. García López²⁹ , M. Garczarczyk⁴² , S. Gasparyan⁶¹, M. Gaug⁵⁹ , N. Giglietto⁵⁴ , F. Giordano⁵⁴ , P. Gliwny⁴¹ , N. Godinović⁶² , J. G. Green³³ , D. Green³³ , D. Hadasch³⁶ , A. Hahn³³ , T. Hassan⁴⁸ , L. Heckmann³³ , J. Herrera²⁹ , D. Hrupec⁶³ , M. Hütten³⁶ , T. Inada³⁶ , R. Iotov⁵⁶, K. Ishio⁴¹ , Y. Iwamura³⁶, I. Jiménez Martínez⁴⁸ , J. Jormanainen⁵⁷, L. Jouvin³⁵ , D. Kerszberg³⁵ , Y. Kobayashi³⁶ , H. Kubo⁶⁴ , J. Kushida⁶⁵ , A. Lamastra³⁰ , D. Lelas⁶² , F. Leone³⁰ , E. Lindfors⁵⁷ , L. Linhoff³⁷ , S. Lombardi³⁰ , F. Longo^{31,66} , R. López-Coto³⁴ , M. López-Moya³⁹ , A. López-Oramas²⁹ , S. Loporchio⁵⁴ , A. Lorini⁶⁷, B. Machado de Oliveira Fraga⁴⁰ , C. Maggio⁵⁹ , P. Majumdar⁶⁸ , M. Makariev⁶⁹ , G. Maneva⁶⁹ , M. Manganaro⁵⁵ , K. Mannheim⁵⁶ , M. Mariotti³⁴ , M. Martínez³⁵ , A. Mas Aguilar³⁹ , D. Mazin^{33,36} , S. Menchiani⁶⁷, S. Mender³⁷ , S. Mićanović⁵⁵ , D. Miceli³⁴ , T. Miener³⁹ , J. M. Miranda⁶⁷ , R. Mirzoyan³³ , E. Molina⁴⁶ , H. A. Mondal⁶⁸, A. Moralejo³⁵ , D. Morcuende³⁹ , V. Moreno⁵⁹ , T. Nakamori⁷⁰ , C. Nanci³⁰, L. Nava³⁰ , V. Neustroev⁷¹ , M. Nieves Rosillo²⁹ , C. Nigro³⁵ , K. Nilsson⁵⁷ , K. Nishijima⁶⁵ , K. Noda³⁶ , S. Nozaki⁶⁴ , Y. Ohtani³⁶ , T. Oka⁶⁴ , J. Otero-Santos²⁹ , S. Paiano³⁰ , M. Palatiello³¹ , D. Paneque³³ , R. Paoletti⁶⁷ , J. M. Paredes⁴⁶ , L. Pavletić⁵⁵ , P. Peñil³⁹ , M. Persic^{31,72} , M. Pihet³³, P. G. Prada Moroni⁴⁵ , E. Prandini³⁴ , C. Priyadarshi³⁵ , I. Puljak⁶² , W. Rhode³⁷ , M. Ribó⁴⁶ , J. Rico³⁵ , C. Righi³⁰ , A. Rugliancich⁴⁵ , N. Sahakyan⁶¹ , T. Saito³⁶ , S. Sakurai³⁶ , K. Satalecka⁴² , F. G. Saturni³⁰ , B. Schleicher⁵⁶ , K. Schmidt³⁷ , F. Schmuckermaier³³, J. L. Schubert³⁷, T. Schweizer³³, J. Sitarek³⁶ , I. Šnidarić⁷³, D. Sobczynska⁴¹ , A. Spolon³⁴ , A. Stamerra³⁰ , J. Strišković⁶³ , D. Strom³³ , M. Strzys³⁶ , Y. Suda⁶⁰ , T. Surić⁷³, M. Takahashi³⁶ , R. Takeishi³⁶ , F. Tavecchio³⁰ , P. Temnikov⁶⁹ , T. Terzić⁵⁵ , M. Teshima^{33,36}, L. Tosti⁷⁴, S. Truzzi⁶⁷, A. Tutone³⁰ , S. Ubach⁵⁹, J. van Scherpenberg³³ , G. Vanzo²⁹ , M. Vazquez Acosta²⁹ , S. Ventura⁶⁷ , V. Verguilov⁶⁹ , I. Viale³⁴ , C. F. Vigorito⁵³ , V. Vitale⁷⁵ , I. Vovk³⁶ , M. Will³³ , C. Wunderlich⁶⁷ , T. Yamamoto⁷⁶ , and D. Zarić⁶² 

(The MAGIC Collaboration)

¹ Physics Department, Columbia University, New York, NY 10027, USA; qifeng@nevis.columbia.edu

² DESY, Platanenallee 6, D-15738 Zeuthen, Germany; contact.magic@mpp.mpg.de

³ Center for Astrophysics | Harvard & Smithsonian, Cambridge, MA 02138, USA

⁴ NASA/Goddard Space Flight Center, Code 661, Greenbelt, MD 20771, USA

⁵ Institute of Physics and Astronomy, University of Potsdam, 14476 Potsdam-Golm, Germany and DESY, Platanenallee 6, D-15738 Zeuthen, Germany

⁶ Department of Physics, Washington University, St. Louis, MO 63130, USA

⁷ Department of Physics and Astronomy, Barnard College, Columbia University, NY 10027, USA

⁸ Physics Department, California Polytechnic State University, San Luis Obispo, CA 94307, USA

⁹ Department of Physics and Astronomy, Purdue University, West Lafayette, IN 47907, USA

¹⁰ Department of Physics and Astronomy and the Bartol Research Institute, University of Delaware, Newark, DE 19716, USA

¹¹ School of Physics and Astronomy, University of Minnesota, Minneapolis, MN 55455, USA

¹² Department of Physics, California State University–East Bay, Hayward, CA 94542, USA

¹³ Department of Physics and Astronomy, Ball State University, Muncie, IN 47306, USA

¹⁴ School of Physics and Center for Relativistic Astrophysics, Georgia Institute of Technology, 837 State Street NW, Atlanta, GA 30332-0430, USA

¹⁵ Physics Department, McGill University, Montreal, QC H3A 2T8, Canada

- ¹⁶ Santa Cruz Institute for Particle Physics and Department of Physics, University of California, Santa Cruz, CA 95064, USA
- ¹⁷ Department of Physics and Astronomy, University of Utah, Salt Lake City, UT 84112, USA
- ¹⁸ Department of Physics and Astronomy, University of Alabama, Tuscaloosa, AL 35487, USA
- ¹⁹ Department of Physics and Astronomy, University of Iowa, Van Allen Hall, Iowa City, IA 52242, USA
- ²⁰ Department of Physics and Astronomy, DePauw University, Greencastle, IN 46135-0037, USA
- ²¹ Department of Physics and Astronomy, Iowa State University, Ames, IA 50011, USA
- ²² School of Physics, National University of Ireland Galway, University Road, Galway, Ireland
- ²³ Department of Physics and Astronomy, Ball State University, Muncie, IN 47306, USA and Department of Physics, Anderson University, 1100 East 5th Street, Anderson, IN 46012, USA
- ²⁴ Department of Physics and Astronomy, University of California, Los Angeles, CA 90095, USA
- ²⁵ School of Physics, University College Dublin, Belfield, Dublin 4, Ireland
- ²⁶ Department of Physical Sciences, Munster Technological University, Bishopstown, Cork, T12 P928, Ireland
- ²⁷ Department of Physics, Indiana University–Purdue University Indianapolis, Indianapolis, IN 46202, USA
- ²⁸ Enrico Fermi Institute, University of Chicago, Chicago, IL 60637, USA
- ²⁹ Instituto de Astrofísica de Canarias and Dpto. de Astrofísica, Universidad de La Laguna, E-38200, La Laguna, Tenerife, Spain
- ³⁰ National Institute for Astrophysics (INAF), I-00136 Rome, Italy
- ³¹ Università di Udine and INFN Trieste, I-33100 Udine, Italy
- ³² Also at International Center for Relativistic Astrophysics (ICRA), Rome, Italy
- ³³ Max-Planck-Institut für Physik, D-80805 München, Germany
- ³⁴ Università di Padova and INFN, I-35131 Padova, Italy
- ³⁵ Institut de Física d'Altes Energies (IFAE), The Barcelona Institute of Science and Technology (BIST), E-08193 Bellaterra (Barcelona), Spain
- ³⁶ Japanese MAGIC Group: Institute for Cosmic Ray Research (ICRR), The University of Tokyo, Kashiwa, 277-8582 Chiba, Japan
- ³⁷ Technische Universität Dortmund, D-44221 Dortmund, Germany
- ³⁸ Croatian MAGIC Group: University of Zagreb, Faculty of Electrical Engineering and Computing (FER), 10000 Zagreb, Croatia
- ³⁹ IPARCOS Institute and EMFTEL Department, Universidad Complutense de Madrid, E-28040 Madrid, Spain
- ⁴⁰ Centro Brasileiro de Pesquisas Físicas (CBPF), 22290-180 URCA, Rio de Janeiro (RJ), Brazil
- ⁴¹ University of Lodz, Faculty of Physics and Applied Informatics, Department of Astrophysics, 90-236 Lodz, Poland
- ⁴² Deutsches Elektronen-Synchrotron (DESY), D-15738 Zeuthen, Germany
- ⁴³ ETH Zürich, CH-8093 Zürich, Switzerland
- ⁴⁴ Instituto de Astrofísica de Andalucía-CSIC, Glorieta de la Astronomía s/n, E-18008, Granada, Spain
- ⁴⁵ Università di Pisa and INFN Pisa, I-56126 Pisa, Italy
- ⁴⁶ Universitat de Barcelona, ICCUB, IEEC-UB, E-08028 Barcelona, Spain
- ⁴⁷ Armenian MAGIC Group: A. Alikhanyan National Science Laboratory, 0036 Yerevan, Armenia
- ⁴⁸ Centro de Investigaciones Energéticas, Medioambientales y Tecnológicas, E-28040 Madrid, Spain
- ⁴⁹ Department for Physics and Technology, University of Bergen, Norway
- ⁵⁰ Now at University of Innsbruck, Austria
- ⁵¹ INFN MAGIC Group: INFN Sezione di Catania and Dipartimento di Fisica e Astronomia, University of Catania, I-95123 Catania, Italy
- ⁵² Also at Port d'Informació Científica (PIC), E-08193 Bellaterra (Barcelona), Spain
- ⁵³ INFN MAGIC Group: INFN Sezione di Torino and Università degli Studi di Torino, I-10125 Torino, Italy
- ⁵⁴ INFN MAGIC Group: INFN Sezione di Bari and Dipartimento Interateneo di Fisica dell'Università e del Politecnico di Bari, I-70125 Bari, Italy
- ⁵⁵ Croatian MAGIC Group: University of Rijeka, Department of Physics, 51000 Rijeka, Croatia
- ⁵⁶ Universität Würzburg, D-97074 Würzburg, Germany
- ⁵⁷ Finnish MAGIC Group: Finnish Centre for Astronomy with ESO, University of Turku, FI-20014 Turku, Finland
- ⁵⁸ Now at Ruhr-Universität Bochum, Fakultät für Physik und Astronomie, Astronomisches Institut (AIRUB), D-44801 Bochum, Germany
- ⁵⁹ Departament de Física, and CERES-IEEC, Universitat Autònoma de Barcelona, E-08193 Bellaterra, Spain
- ⁶⁰ Japanese MAGIC Group: Physics Program, Graduate School of Advanced Science and Engineering, Hiroshima University, 739-8526 Hiroshima, Japan
- ⁶¹ Armenian MAGIC Group: ICRA Net-Armenia at NAS RA, 0019 Yerevan, Armenia
- ⁶² Croatian MAGIC Group: University of Split, Faculty of Electrical Engineering, Mechanical Engineering and Naval Architecture (FESB), 21000 Split, Croatia
- ⁶³ Croatian MAGIC Group: Josip Juraj Strossmayer University of Osijek, Department of Physics, 31000 Osijek, Croatia
- ⁶⁴ Japanese MAGIC Group: Department of Physics, Kyoto University, 606-8502 Kyoto, Japan
- ⁶⁵ Japanese MAGIC Group: Department of Physics, Tokai University, Hiratsuka, 259-1292 Kanagawa, Japan
- ⁶⁶ Also at Dipartimento di Fisica, Università di Trieste, I-34127 Trieste, Italy
- ⁶⁷ Università di Siena and INFN Pisa, I-53100 Siena, Italy
- ⁶⁸ Saha Institute of Nuclear Physics, HBNI, 1/AF Bidhannagar, Salt Lake, Sector-1, Kolkata 700064, India
- ⁶⁹ Inst. for Nucl. Research and Nucl. Energy, Bulgarian Academy of Sciences, BG-1784 Sofia, Bulgaria
- ⁷⁰ Japanese MAGIC Group: Department of Physics, Yamagata University, Yamagata 990-8560, Japan
- ⁷¹ Finnish MAGIC Group: Astronomy Research Unit, University of Oulu, FI-90014 Oulu, Finland
- ⁷² Also at INAF Trieste and Dept. of Physics and Astronomy, University of Bologna, Bologna, Italy
- ⁷³ Croatian MAGIC Group: Ruđer Bošković Institute, 10000 Zagreb, Croatia
- ⁷⁴ INFN MAGIC Group: INFN Sezione di Perugia, I-06123 Perugia, Italy
- ⁷⁵ INFN MAGIC Group: INFN Roma Tor Vergata, I-00133 Roma, Italy
- ⁷⁶ Japanese MAGIC Group: Department of Physics, Konan University, Kobe, Hyogo 658-8501, Japan

Received 2022 January 21; revised 2022 May 4; accepted 2022 May 5; published 2022 June 27

Abstract

We report on a long-lasting, elevated gamma-ray flux state from VER J0521+211 observed by VERITAS, MAGIC, and Fermi-LAT in 2013 and 2014. The peak integral flux above 200 GeV measured with the nightly binned light curve is $(8.8 \pm 0.4) \times 10^{-7}$ photons $\text{m}^{-2} \text{s}^{-1}$, or $\sim 37\%$ of the Crab Nebula flux. Multiwavelength observations from X-ray, UV, and optical instruments are also presented. A moderate correlation between the



Original content from this work may be used under the terms of the [Creative Commons Attribution 4.0 licence](https://creativecommons.org/licenses/by/4.0/). Any further distribution of this work must maintain attribution to the author(s) and the title of the work, journal citation and DOI.

X-ray and TeV gamma-ray fluxes was observed, and the X-ray spectrum appeared harder when the flux was higher. Using the gamma-ray spectrum and four models of the extragalactic background light (EBL), a conservative 95% confidence upper limit on the redshift of the source was found to be $z \leq 0.31$. Unlike the gamma-ray and X-ray bands, the optical flux did not increase significantly during the studied period compared to the archival low-state flux. The spectral variability from optical to X-ray bands suggests that the synchrotron peak of the spectral energy distribution (SED) may become broader during flaring states, which can be adequately described with a one-zone synchrotron self-Compton model varying the high-energy end of the underlying particle spectrum. The synchrotron peak frequency of the SED and the radio morphology of the jet from the MOJAVE program are consistent with the source being an intermediate-frequency-peaked BL Lac object.

Unified Astronomy Thesaurus concepts: Active galactic nuclei (16); High energy astrophysics (739); Blazars (164); BL Lacertae objects (158); Relativistic jets (1390); Gamma-rays (637); Non-thermal radiation sources (1119)

1. Introduction

Blazars are divided into subclasses: high-frequency-peaked BL Lac objects (HBLs), intermediate-frequency-peaked BL Lac objects (IBLs), low-frequency-peaked BL Lac objects (LBLs), and flat-spectrum radio quasars (FSRQs), based on the peak frequency of their spectral energy distribution (SED) and the equivalent width of optical emission lines (e.g., Urry & Padovani 1995). TeV gamma rays have been detected from all subclasses of blazars, predominantly from HBLs. A few IBLs/LBLs have also been detected in the TeV gamma-ray band, most frequently during flaring states (e.g., Arlen et al. 2013; MAGIC Collaboration et al. 2018), including VER J0521+211 (Archambault et al. 2013).

Interesting differences in radio morphology between subclasses of blazars, beyond the well-known “blazar sequence” (Fossati et al. 1998), have been recently proposed (e.g., Kharb et al. 2008; Hervet et al. 2016). Particularly, some blazars, typically belonging to the IBL/LBL subclass, exhibit a combination of stationary knots and superluminal knots in their jets as observed with the Very Long Baseline Array (VLBA). Gamma-ray flares contemporaneous with the ejection of superluminal knots have been observed in a few TeV IBLs (e.g., Arlen et al. 2013; Abeysekara et al. 2018; MAGIC Collaboration et al. 2018), providing tantalizing evidence for recollimation shocks (e.g., Komissarov & Falle 1998; Narayan et al. 2009).

The discovery of VER J0521+211 in the TeV gamma-ray band was made from VERITAS observations of the radio and X-ray source RGB J0521.8+2112, motivated by a cluster of photons with energies >30 GeV in Fermi-LAT data (Archambault et al. 2013). The positions of the source determined with X-ray, GeV, and TeV gamma-ray data are all within $0^{\circ}.1$. The spatial association across the electromagnetic spectrum and correlated variability, most prominent between X-ray and gamma-ray bands, strongly support the association between VER J0521+211 and RGB J0521.8+2112.

As is the case with many other BL Lac objects, the lack of optical emission features leads to a redshift uncertainty of the source. A redshift of $z=0.108$ was reported by Shaw et al. (2013), but later studies were unable to confirm it (Archambault et al. 2013; Paiano et al. 2017). Instead, a lower limit of $z > 0.18$ (Paiano et al. 2017) and an upper limit of $z < 0.34$ (Archambault et al. 2013) were reported.

VER J0521+211 is classified as an IBL, as the peak of its SED in a low state lies between 10^{14} and 10^{15} Hz. However, the source exhibits a harder X-ray spectrum and HBL-like behavior during flares (Archambault et al. 2013). In HBLs, it is particularly interesting to study the flux correlation between

X-ray and TeV gamma-ray bands, where the SED peaks lie. Despite being model dependent, the quantitative description of the correlation between X-rays and TeV gamma rays can be informative of the radiative processes of the relativistic particles (e.g., Katarzyński et al. 2005). For example, a particle injection in a one-zone synchrotron self-Compton (SSC) model in the Thomson regime would lead to a quadratic correlation between the gamma-ray and X-ray flux, but it could lead to a linear correlation if the inverse Compton (IC) scattering happens in the deep Klein–Nishina (KN) regime (e.g., Aleksić et al. 2015; Baloković et al. 2016).

In this work, we report on the results from multiwavelength (MWL) observations of the blazar VER J0521+211 between 2012 November and 2014 February, focusing on the TeV gamma-ray and X-ray behaviors.

2. Observations and Data Analysis

2.1. Veritas

The Very Energetic Radiation Imaging Telescope Array System (VERITAS) is an array of four imaging atmospheric Cerenkov telescopes (IACTs) located in southern Arizona ($30^{\circ}40'N$, $110^{\circ}57'W$, 1.3 km a.s.l.; Park & The VERITAS Collaboration 2015). It is sensitive to gamma rays in the energy range from 85 GeV to >30 TeV with an energy resolution of $\sim 15\%$ (at 1 TeV). The angular resolution (68% containment at 1 TeV) is $\sim 0^{\circ}.1$. VERITAS is capable of making a detection at a statistical significance of 5 standard deviations (5σ) of a point source of 1% Crab Nebula flux in ~ 25 hr, with an energy threshold of 240 GeV when a set of a priori data selection cuts optimized on sources with a moderate power-law index (from -2.5 to -3) is used.

After its initial discovery in the TeV band (Archambault et al. 2013), VER J0521+211 was observed again by VERITAS from 2012 November to 2014 February, with a total exposure of 23.6 hr after data quality selection and dead-time correction. We analyzed the data using two independent analysis packages (Cogan 2008; Maier & Holder 2017), with a priori cuts optimized for lower-energy showers (see, e.g., Archambault et al. 2014). The results of both analyses are compatible, and here we use the analysis package described in Cogan (2008).

2.2. Magic

MAGIC is an array of two IACTs located on the Canary Island of La Palma ($28^{\circ}45'43''N$, $17^{\circ}53'24''W$, 2.2 km a.s.l.; Aleksić et al. 2016). MAGIC is capable of detecting a point source of $\sim 0.7\%$ of the Crab Nebula flux above 220 GeV in

~ 50 hr with a statistical significance of 5σ (Aleksić et al. 2016). Above 220 GeV, its energy resolution is $\sim 16\%$ and its angular resolution (68% containment) is $\lesssim 0.07^\circ$.

VER J0521+211 was observed by MAGIC on four nights between 2013 October and 2013 December, triggered by elevated optical and GeV gamma-ray fluxes (Buson 2013). After data quality selection and dead-time correction, a total effective time of ~ 4.5 hr was taken on 2013 October 15, October 16, November 29, and December 2. Details on the stereo analysis of the MAGIC data can be found in Aleksić et al. (2011).

2.3. Fermi-LAT

The Large Area Telescope (LAT) on board the Fermi satellite is a pair-conversion gamma-ray telescope sensitive to energies from ~ 20 MeV to >300 GeV (Atwood et al. 2009).

We performed an unbinned likelihood analysis covering the period of the TeV gamma-ray observations using the LAT ScienceTools v11r5p3 and Pass-8 P8R2_SOURCE_V6_v06 instrument response functions (Atwood et al. 2013). We selected SOURCE class events with an energy between 100 MeV and 300 GeV within 10° from the direction of VER J0521+211, with a maximum zenith-angle cut of 90° . We included all point sources within 20° from the source direction in our model, while only leaving the normalization parameters free for those within 5° from the source, and fixed the parameters to the Fermi Large Area Telescope Third Source Catalog (3FGL; Acero et al. 2015) values for those farther away. We also included the 3FGL Galactic (gll_iem_v06) and isotropic (iso_P8R2_SOURCE_V6_v06) diffuse emission in the model.

2.4. Swift-XRT

The X-Ray Telescope (XRT) on the Neil Gehrels Swift Observatory is a grazing-incidence focusing X-ray telescope, sensitive to energies from 0.2 to 10 keV (Gehrels et al. 2004; Burrows et al. 2005). There were 32 Swift-XRT observations taken on VER J0521+211 in the period of interest, 28 of which were taken in photon-counting (PC) mode between 2013 October and 2014 February, and four in window-timing (WT) mode in 2012 November. We processed these XRT data using xrtpipeline.⁷⁷ We selected photons with an energy between 0.3 and 10 keV and within a circular source region of radius 20 pixels ($\sim 47''/2$) to estimate the flux of the source, while those within an annular background region with inner and outer radii of 70 and 120 pixels ($\sim 2!75 - 4!72$) were selected to estimate the background contribution. For those observations with a count rate in the source region above 0.5 counts s^{-1} , we checked that the point-spread function is well described by the King function (Moretti et al. 2005), and therefore it is not necessary to correct for the pileup effect.

We used an absorbed log-parabola model to fit the X-ray spectrum:

$$\frac{dN}{dE} = e^{-N_H\sigma(E)} K \left(\frac{E}{1 \text{ keV}} \right)^{-\alpha - \beta \log(E/1 \text{ keV})}, \quad (1)$$

where in the absorption component N_H represents the column density of neutral hydrogen and $\sigma(E)$ is the photoelectric cross

section, while in the power-law component K is the normalization, α is the photon index at 1 keV, and β describes the spectral curvature, i.e., the energy dependence of the photon index. We fixed the value of N_H to the total neutral hydrogen density, $N_H = 4.38 \times 10^{21} \text{ cm}^{-2}$, derived from the Leiden/Argentine/Bonn (LAB) survey of Galactic HI (Kalberla et al. 2005), following Willingale et al. (2013).

2.5. Swift-UVOT

The Swift-Ultraviolet/Optical telescope (UVOT; Roming et al. 2005) was used in some of the observations of VER J0521+211 during the time period of interest. The counts from the source were extracted from an aperture with a radius of $5.0''$ centered on the position of the source, and the background counts were estimated using the counts from four neighboring regions without any bright source, each having the same radius. The magnitude of the source was then computed using uvotsource,⁷⁸ and it was later converted to flux using the zero-point for each of the UVOT filters (the central wavelengths of which are V 5468 Å, B 4392 Å, U 3465 Å, UVW1 2600 Å, UVM2 2246 Å, and UVW2 1928 Å) from Poole et al. (2008).

An extinction correction was applied following the procedure described in Roming et al. (2009), using the value of $E(B - V) = 0.605$ (Schlafly & Finkbeiner 2011). Since VER J0521+211 is located close to the Galactic plane, with a Galactic latitude of -8.7° , the uncertainty on the dust extinction is large. A reddening value of $E(B - V) = 0.703$ was found for the direction toward VER J0521+211 using 472 elliptical galaxies to calibrate infrared dust maps (Schlegel et al. 1998). The value $E(B - V) = 0.605$ used in this work was derived more recently using 261,496 stars from the Sloan Digital Sky Survey (Schlafly & Finkbeiner 2011), which is 14% lower than the value from Schlegel et al. (1998). Schlafly & Finkbeiner (2011) pointed out that if substantial dust exists beyond a distance of 6 kpc, the reddening and extinction would be underestimated.

2.6. Steward Observatory

VER J0521+211 was monitored in the V band by the Steward Observatory (Smith et al. 2009). There were 76 observations on 37 nights between 2013 November 25 and 2014 April 1. In this work we use the V -band polarimetry results that are publicly available.⁷⁹

3. Results

3.1. Temporal Variability

3.1.1. Gamma-Ray Light Curves

From the VERITAS observations between 2012 November and 2013 February, which yielded a quality-selected live time of 4.6 hr, the source was detected at a statistical significance of 18σ at a time-averaged integral flux above 200 GeV of $(2.4 \pm 0.2) \times 10^{-7}$ photons $m^{-2} s^{-1}$. From the 16.4 hr of observations between 2013 October and 2014 February, the source was detected at 62σ and $(3.9 \pm 0.1) \times 10^{-7}$ photons $m^{-2} s^{-1}$ above 200 GeV.

⁷⁷ HEASOFT v6.23, swxrtdas_23Jan18_v3.4.1, with calibrations from the database CALDB 20171113.

⁷⁸ HEASOFT v6.23, with calibrations from the database CALDB 20170922.
⁷⁹ <http://james.as.arizona.edu/~psmith/Fermi>

An overall statistical significance of 30.5σ was obtained from the analysis of the MAGIC observations on the four nights during the period of interest. The energy threshold of these observations was estimated to be ~ 65 GeV. The average flux above 200 GeV of these four MAGIC observations is $(5.8 \pm 1.0) \times 10^{-7}$ photons $\text{m}^{-2} \text{s}^{-1}$.

The TeV gamma-ray light curve (>200 GeV) of VER J0521+211 measured by VERITAS and MAGIC is shown in the top panel of Figure 1. The TeV gamma-ray flux of the source was variable between 2013 October and 2014 February (see the top panel of Figure 2), as a best-fit constant-flux model gives a χ^2 value of 442.4 with 19 degrees of freedom (dof), resulting in a negligible p -value. However, a fit of the TeV gamma-ray flux on the five nights with VERITAS observations between 2012 November and 2013 February to a constant-flux model yields a χ^2 value of 9.1 with 4 dof, equivalent to a p -value of 0.59. Therefore, we do not rule out constant flux from the source in late 2012 through early 2013.

The TeV gamma-ray flux above 200 GeV reached a peak of $(8.8 \pm 0.4) \times 10^{-7}$ photons $\text{m}^{-2} \text{s}^{-1}$ ($\sim 37\%$ of the Crab Nebula flux), as measured by VERITAS on the night of 2013 December 3. No intraday variability was found in the VERITAS data obtained on the night of the peak flux. On 2013 December 2, the night immediately before the peak TeV flux, MAGIC measured a lower flux above 200 GeV of $(5.1 \pm 0.9) \times 10^{-7}$ photons $\text{m}^{-2} \text{s}^{-1}$.

The monthly binned GeV gamma-ray light curve measured by Fermi-LAT between 2012 October and 2014 May is shown in the second panel of Figures 1 and 2. A fit of the GeV gamma-ray light curve to a constant-flux model yields a χ^2 value of 102.5 with dof = 22, equivalent to a negligible p -value, showing that the source was variable during the period of interest. The average flux value during the 1 yr period between 2013 January 29 and 2014 January 24 was about 11 times that from the 3FGL catalog (illustrated by the horizontal dashed lines in Figures 1 and 2), and the monthly flux stayed above 7 times the 3FGL catalog value, indicating a long-lasting elevated GeV gamma-ray flux state. During the period between 2013 October and 2014 February, when most of the observations at TeV gamma-ray and X-ray energies were performed, the GeV gamma-ray flux of the source did not show significant variability on monthly timescales.

3.1.2. Bayesian Blocks from the Gamma-Ray Light Curves

A Bayesian block analysis (Scargle et al. 2013) of the TeV gamma-ray light curve was performed using the Python package Astropy (Astropy Collaboration et al. 2013, 2018), with an empirical prior equivalent to a false-alarm probability $p_0 = 3 \times 10^{-7}$. Two change points (i.e., the edges of the Bayesian blocks), 2013 December 2 and 2013 December 6, were obtained from the VERITAS and MAGIC flux measurements, as illustrated by the light-blue vertical dashed lines in Figures 1 and 2. These two change points define three Bayesian blocks, designated as BB1, BB2, and BB3, within each of which the flux is consistent with being constant and no variability is detected above 5σ statistical significance. The date ranges and the average fluxes of the three Bayesian blocks are shown in Table 1. Note that there was only one night with 2.3 hr of VERITAS observations on 2013 December 3 in the BB2 interval, with an averaged flux above 200 GeV of $(8.8 \pm 0.4) \times 10^{-7}$ photons $\text{m}^{-2} \text{s}^{-1}$ ($\sim 37\%$ of the Crab Nebula flux), the highest of all three Bayesian blocks. The flux in BB3 is comparable to that in 2012,

$(2.4 \pm 0.2) \times 10^{-7}$ photons $\text{m}^{-2} \text{s}^{-1}$. MWL SEDs were constructed for the three time intervals from the Bayesian block analysis of the TeV gamma-ray light curve (see Section 3.2).

The same Bayesian block analysis was performed for the monthly binned Fermi-LAT light curve. Two change points were found in the GeV flux of the source, 2013 January 29 and 2014 January 24. The GeV gamma-ray flux remained roughly constant in the year 2013, before and after which the flux tapered off.

3.1.3. X-ray and UV/Optical Light Curves and Fractional Variability

The light curves measured by Swift-XRT, Swift-UVOT, and the Steward Observatory are shown in the lower panels of Figures 1 and 2. The flux of the source at all of the studied wavelengths, as well as the electric vector position angle (EVPA) and the polarization fraction in the optical V band, exhibited variability during the period of interest.

To examine the relative variability amplitude at different wavelengths, the fractional variability amplitude F_{var} (Vaughan et al. 2003; Poutanen et al. 2008) as a function of frequency is shown in Figure 3. The measured F_{var} value calculated from each light curve is shown in Table 2. The VHE flux exhibits the highest fractional variability amplitude of $F_{\text{var}} = 0.54 \pm 0.03$ among all of the observed frequencies, with the X-ray flux yielding the second-highest $F_{\text{var}} = 0.45 \pm 0.02$. The F_{var} values in the optical and UV bands are the lowest.

It is worth noting that F_{var} depends on the timescales, both long (duration) and short (bin width), of the light curve. A wider sampling coverage of the same light curve with a smaller bin width and a longer duration will generally increase F_{var} . The durations of the light curves used to calculate F_{var} are similar; so are the bin widths, with the exception of the monthly binned Fermi-LAT light curve.

3.1.4. Optical Polarization Variability

Significant variability in both the EVPA and the polarization fraction was observed. The V-band EVPA roughly ranges between 25° and 50° during the time when TeV gamma-ray observations were taken. The jet position angle from radio observations was measured in late 2012 and early 2014 to range from around 287° for the innermost feature at ~ 5 mas (from the core) down to about 240° for the outermost feature at ~ 50 mas (Lister et al. 2019). The polarization fraction varied between around 4% and almost 12%. On 2013 December 3 (the night with the highest TeV gamma-ray flux measured with VERITAS), a small increase in polarization fraction from $9.47\% \pm 0.08\%$ to $11.03\% \pm 0.45\%$ was observed. The fractional variability amplitudes F_{var} of the V-band polarization fraction and EVPA are 0.178 ± 0.001 and 0.244 ± 0.001 , respectively. Changes in polarization fraction were also observed about a month later, with possibly associated variability in X-ray and optical/UV fluxes around MJD 56660, but without significant flux elevation in the VHE band. Therefore, it is inconclusive whether or not the EVPA rotation and polarization fraction changes are associated with the gamma-ray variability.

It is worth noting that the behavior of the optical polarization of this source around the time of high TeV gamma-ray flux is quite different from the dramatic swing of the EVPA during some major gamma-ray flares observed for high-power blazars (see, e.g., Abdo et al. 2010). In those cases, a fast swing of the EVPA by 90° or 180° accompanied by a decrease (almost to 0)

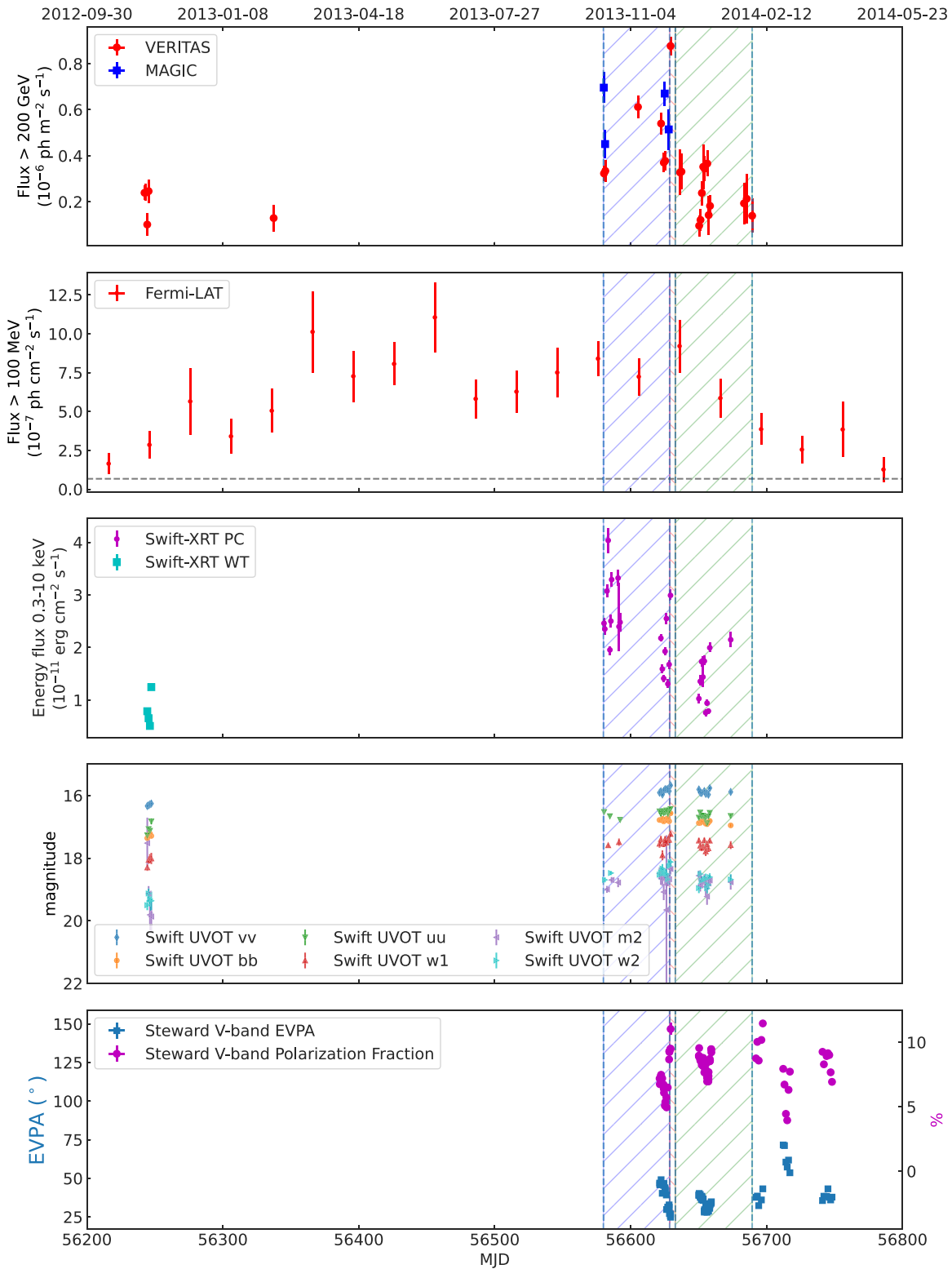


Figure 1. MWL light curves of VER J0521+211 of the entire period of interest in this work, from late 2012 to early 2014. The vertical dashed lines and the colored hatch fills illustrate the three Bayesian blocks between late 2013 and early 2014, based on which we selected the three periods for SED modeling. The binning of the light curves is nightly for VERITAS and MAGIC, monthly for Fermi-LAT, and by observations for Swift and Steward Observatory. Only 1σ statistical uncertainties are shown.

of the polarization fraction was observed during a major GeV gamma-ray flare. However, the relation between EVPA rotations, polarization fractions, and gamma-ray flares in BL Lac objects appears to differ from case to case (see, e.g., Arlen et al. 2013; MAGIC Collaboration et al. 2019).

3.2. Spectral Variability

3.2.1. VHE Gamma-Ray Spectrum

The VERITAS spectra during the three periods BB1—BB3, as defined in Section 3.1.2, are shown in Figure 4. No evidence

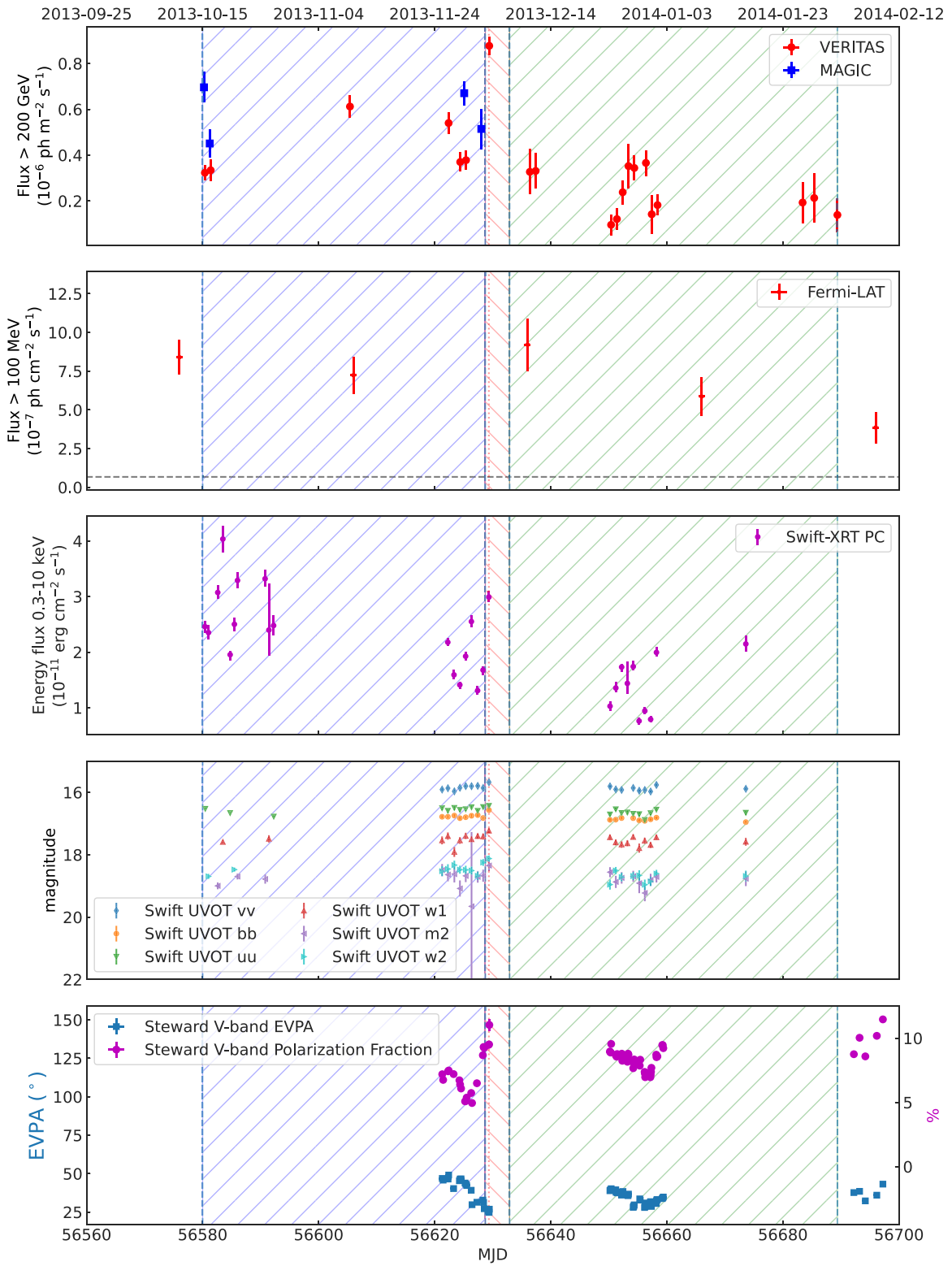


Figure 2. MWL light curves of VER J0521+211 focusing on the data between late 2013 and early 2014. The vertical dashed lines and the hatch fills illustrate the three Bayesian blocks (blue, red, and green, sequentially). The date ranges of the Bayesian blocks are listed in Table 1. The vertical red dotted line illustrates the one night with the highest TeV gamma-ray flux, during which activity at other wavelengths can also be seen. Only 1σ statistical uncertainties are shown.

of spectral variability was observed between these flux states, despite the integrated flux being different by a factor of four. The best-fit spectral parameters for a power-law model and a log-parabola model ($N_0(E/300 \text{ GeV})^{[-\alpha - \beta \log_{10}(E/300 \text{ GeV})]}$) for the three Bayesian blocks are shown in Table 3. The curved log-parabola model describes the spectra during BB1 and BB2

better than a power-law model. During the highest flux, in BB2, the VERITAS spectrum of the source extended beyond 1 TeV without any evidence of a sharp cutoff.

The MAGIC spectra measured on three of the four nights, 2013 October 15, October 16, and November 29, are shown in Figure 5, together with a log-parabola fit. The best-fit spectral

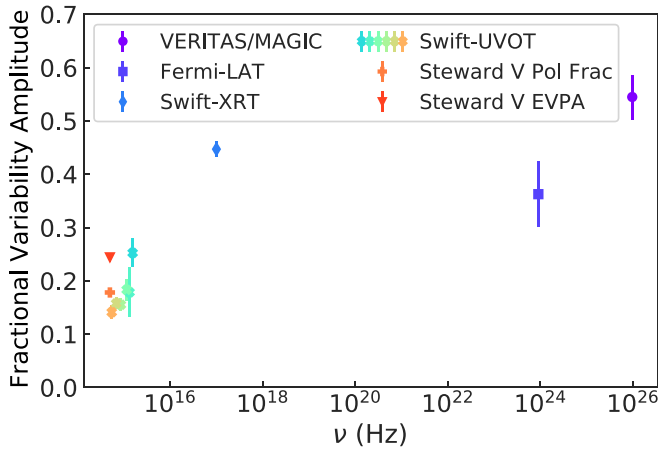


Figure 3. Fractional variability amplitude (F_{var}) as a function of frequency computed from the light curves shown in Figure 1. The filled circle is calculated from the nightly binned VHE light curve, the filled square is from the monthly binned Fermi-LAT light curve, the filled diamond is from the Swift-XRT light curve binned by observations, the filled crosses are from the Swift-UVOT light curves with the six filters binned by observations, and the filled plus sign and downward-pointing triangle are from the V -band polarization fraction and EVPA measured by the Steward Observatory, respectively.

Table 1

Bayesian Blocks Calculated from the TeV Gamma-ray Light Curve Shown in Figure 1

Period	Start (MJD)	End (MJD)	Flux (>200 GeV) (10^{-7} photons $\text{m}^{-2} \text{s}^{-1}$)
BB1	56580.0	56628.5	4.1 ± 0.1
BB2	56628.5	56632.5	8.8 ± 0.4
BB3	56632.5	56689.0	2.7 ± 0.2

parameters and reduced χ^2 values for these three nights are shown in Table 3. Note that the MAGIC spectra extend down to a lower energy (70 GeV) than those from VERITAS, thanks to the larger areas of the reflectors, capturing slightly more spectral curvature at low energies.

3.2.2. X-Ray and UV/Optical Spectral Variability

The X-ray spectrum from each Swift-XRT observation was extracted. The detailed information of these observations and the results of the spectral fits are shown in Table 5 in the Appendix. The relation between the best-fit photon index at 2 keV ($\alpha + \beta \log 2$) and the energy flux in XRT data is illustrated by Figure 6. The log-parabola energy-dependent photon index at 2 keV is comparable to the power-law index for this source and therefore chosen to investigate the X-ray index–flux correlation. A “harder-when-brighter” trend, i.e., a smaller photon index when the flux is higher, is apparent. The Pearson correlation coefficient between the index and flux is 0.76 (p -value $\sim 6 \times 10^{-7}$). A linear fit yields a slope of -0.2 ± 0.04 .

A combined analysis was performed using observations taken during each of the three Bayesian blocks. The best-fit power-law model suggests that the X-ray spectrum during the last Bayesian block was marginally softer (with an index at 2 keV of 2.73 ± 0.11) than that for the first Bayesian block (with an index at 2 keV of 2.57 ± 0.06).

The UV/optical spectrum of the source can be obtained by combining the extinction-corrected fluxes at the six wavelengths

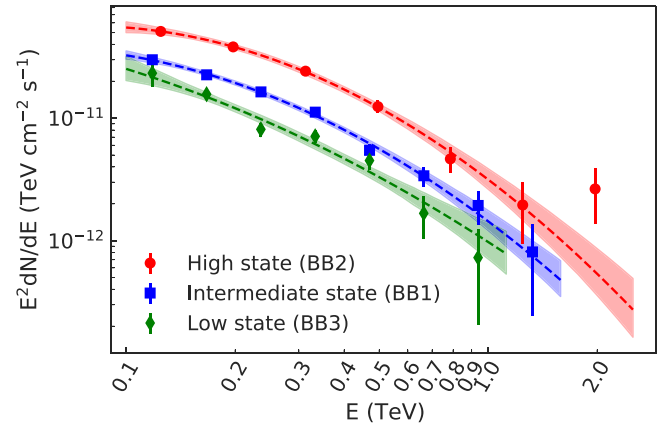


Figure 4. The VERITAS gamma-ray spectra of VER J0521+211 during three different flux states. The dashed lines show the best-fit log-parabola models for the spectra. The 1σ uncertainties from the model parameters are shown in shaded colors. These flux states were chosen based on a Bayesian block analysis of the VERITAS TeV gamma-ray light curve.

Table 2

Fractional Variability Calculated from the MWL Light Curves Shown in Figure 1

Instrument	F_{var}
VERITAS and MAGIC	0.54 ± 0.03
Fermi-LAT	0.36 ± 0.06
Swift-XRT (PC)	0.38 ± 0.02
Swift-XRT (WT)	0.34 ± 0.02
Swift-XRT (combined)	0.45 ± 0.02
Swift-UVOT (UWV2)	0.25 ± 0.03
Swift-UVOT (UVM2)	0.18 ± 0.05
Swift-UVOT (UWV1)	0.18 ± 0.02
Swift-UVOT (U)	0.16 ± 0.01
Swift-UVOT (B)	0.16 ± 0.01
Swift-UVOT (V)	0.14 ± 0.01
Steward Observatory (Pol. Frac.)	0.178 ± 0.001
Steward Observatory (EVPA)	0.244 ± 0.001

Table 3

VHE Gamma-Ray Spectral Fit Parameters Using Power-law and Log-parabola Models

	Power Law		Log Parabola		
	Γ	χ^2/dof	α	β	χ^2/dof
VERITAS BB1	3.2 ± 0.1	4.3	3.2 ± 0.1	1.0 ± 0.3	0.8
VERITAS BB2	3.1 ± 0.1	3.2	3.1 ± 0.1	0.9 ± 0.2	0.5
VERITAS BB3	3.4 ± 0.1	1.6	3.1 ± 0.1	0.5 ± 0.5	1.7
MAGIC October 15	3.0 ± 0.1	5.9	3.7 ± 0.2	1.9 ± 0.4	0.4
MAGIC October 16	2.9 ± 0.2	0.8	3.1 ± 0.3	0.8 ± 0.7	0.6
MAGIC November 29	3.1 ± 0.1	8.5	3.7 ± 0.2	1.7 ± 0.3	1.1

from the Swift-UVOT filtered observations. However, the uncertainty in the measured reddening affects the extinction correction, most notably in the UV band, and subsequently affects the interpretation of the frequency of the synchrotron peak in the broadband SED. If the true reddening is closer to the value $E(B - V) = 0.703$ from Schlegel et al. (1998), the frequency of the synchrotron peak of the SED would be above the UV band, making this source an HBL during the flaring state.

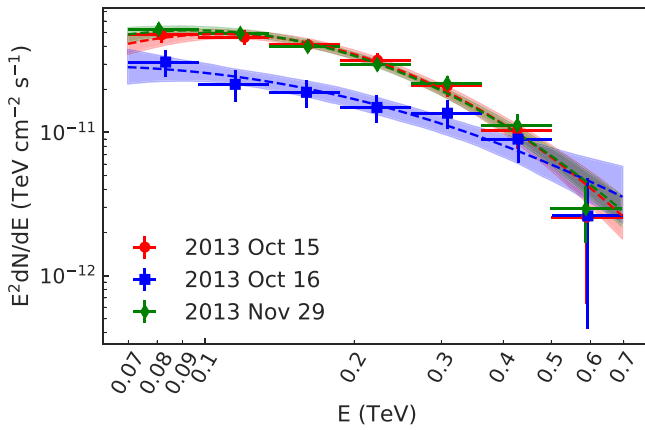


Figure 5. The MAGIC gamma-ray spectra of VER J0521+211 from observations on three nights in 2013. The dashed lines show the best-fit log-parabola models.

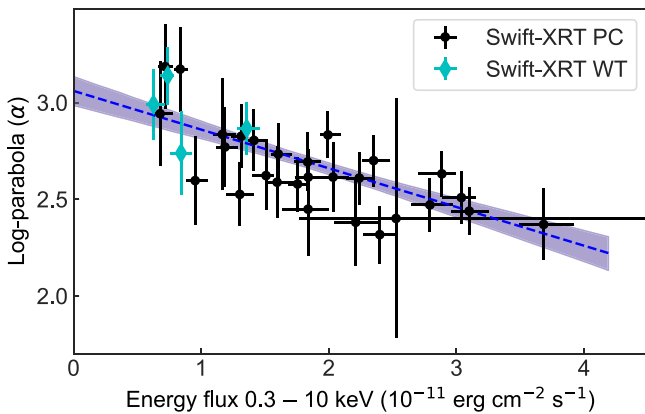


Figure 6. Scatter plot to investigate the correlation between the best-fit X-ray photon index at 2 keV and the X-ray energy flux. The blue dashed line shows the best-fit linear model.

However, if the true reddening is the value $E(B - V) = 0.605$ from Schlafly & Finkbeiner (2011), as we used in this work, the frequency of the synchrotron peak would be below 10^{15} Hz, still in the IBL regime.

Because of the uncertainty in the measured reddening, we did not include data taken with the two Swift-UVOT filters with the highest frequencies in the UV/optical spectra. The UVOT spectra at the lower four frequencies during the three periods were fitted with a power-law model to estimate the spectral variability. The UV spectrum is marginally harder during BB2, with a best-fit index of 2.23 ± 0.09 , whereas those during BB1 and BB3 are 2.41 ± 0.06 and 2.37 ± 0.05 , respectively. This is consistent with the “harder-when-brighter” behavior in the X-ray band. Because the extinction correction is the same for all periods, the relative change is robust against the chosen reddening value.

3.2.3. X-Ray/Gamma-Ray Correlation

A moderate correlation between TeV gamma-ray and X-ray fluxes observed within a 1-day window is apparent, as shown in Figure 7, with a Pearson correlation coefficient r between the two bands of 0.74 (p -value 0.0014). Note that the small number of data points and the potential non-Gaussian distribution of the observed fluxes of the source make it hard to interpret the Pearson’s r correlation. A linear fit, a quadratic fit, and a

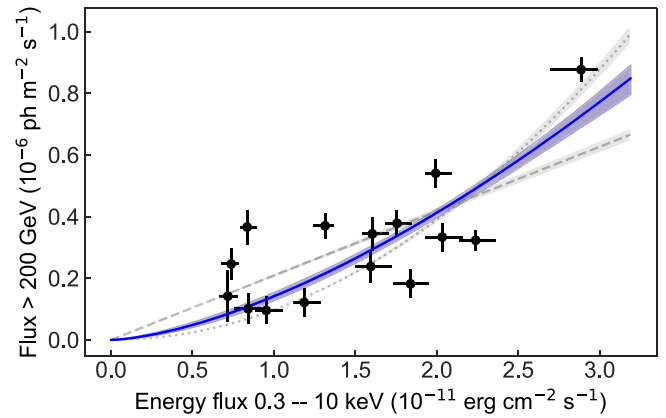


Figure 7. Scatter plot to investigate the correlation between the TeV gamma-ray flux and the X-ray energy flux. The flux measurements in the two bands were performed on the same nights. The gray dashed and dotted lines show the best linear and quadratic fits, respectively. The solid blue line shows the best power-law fit.

power-law fit ($F_{\text{TeV}} \propto F_X^a$) were performed. All three models yielded rather large reduced χ^2 values (between 8.4 and 9.6), likely due to the intrinsic scatter of the gamma-ray/X-ray correlation. The best-fit power-law index is $a = 1.55 \pm 0.12$, indicating that the correlation between TeV gamma-ray and X-ray fluxes is likely between quadratic ($a = 2$) and linear ($a = 1$).

3.2.4. Optical-UV/Gamma-Ray Correlation

The correlations between the TeV gamma-ray flux and the optical/UV energy fluxes measured with the six Swift-UVOT filters are shown in Figure 8. The Pearson correlation coefficients range between 0.47 and 0.76 (the p -values range between 0.01 and 0.08 except for the UVW2 filter), reaching the highest value of 0.76 (p -value of 0.0015) between the UV flux observed with the highest-frequency UVW2 filter and the TeV gamma rays (as shown in the bottom right panel of Figure 8). A power-law fit ($F_{\text{TeV}} \propto F_{\text{UVOT}}^b$) indicates a more-than-quadratic relation with indices $b > 2$ between these bands, although the goodness of fit is poor with reduced χ^2 values ranging between 6.4 (between UVW2 and VHE) and 16.7 (between UVM2 and VHE). However, the fractional variability amplitudes F_{var} in the optical/UV bands are much lower than in the VHE and X-ray bands, increasing with frequency from 0.14 ± 0.01 for the lowest-frequency V filter to 0.25 ± 0.03 for the highest-frequency UVW2 filter, as shown in Figure 3. The low F_{var} values for optical/UV fluxes would generally lead to a steeper optical/UV/VHE correlation with a large index b . We note that the F_{var} values are not affected by extinction correction.

3.3. Broadband SED

The broadband SEDs were constructed for the three Bayesian block intervals, BB1, BB2, and BB3, and are shown in Figure 9. The EBL absorption of the VHE gamma-ray spectra was considered following Franceschini et al. (2008), assuming a redshift of $z = 0.18$ (Paiano et al. 2017). The X-ray spectra were corrected for the neutral hydrogen absorption (see Section 2.4). The UV/optical spectra were corrected for extinction (see Section 2.5). The SEDs are modeled with a one-zone SSC model as described below in Section 4.4.

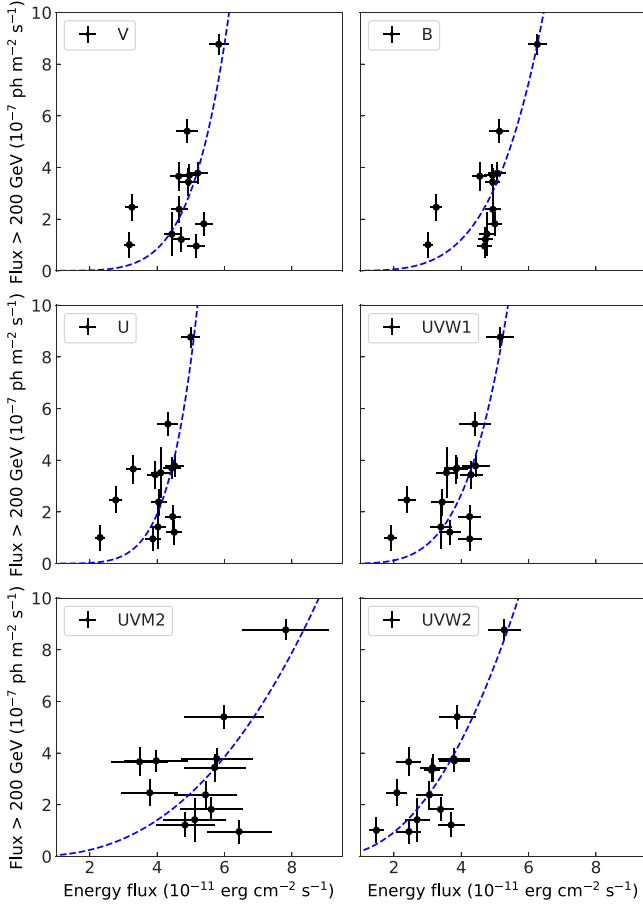


Figure 8. The correlations between the TeV gamma-ray flux and the optical/UV energy fluxes measured with the six Swift-UVOT filters. The frequency of the Swift-UVOT observations increases from the top left panel to the bottom right panel. Similar to Figure 7, the flux measurements in the two bands in each panel were performed on the same nights. The blue dashed lines show the best-fit power law to guide the eye.

4. Discussion

4.1. Flux Variability

The blazar VER J0521+211 was observed at an elevated gamma-ray state between 2013 and 2014 with VERITAS, MAGIC, and Fermi-LAT. The TeV gamma-ray flux above 200 GeV reached a peak of $(8.8 \pm 0.4) \times 10^{-7}$ photons $\text{m}^{-2} \text{s}^{-1}$ ($\sim 37\%$ of the Crab Nebula flux) on the night of 2013 December 3. The MAGIC observations on 2013 December 2, 1 day before the night of the peak TeV gamma-ray flux, yielded a flux above 200 GeV of $(5.1 \pm 0.9) \times 10^{-7}$ photons $\text{m}^{-2} \text{s}^{-1}$, implying variability on a daily timescale. The GeV gamma-ray flux above 100 MeV stayed above 5 times the value from 3FGL for over 5 months between 2013 September and 2014 February, with an average flux of 10 times the 3FGL value.

MWL variability from the optical to VHE bands was observed in 2013 and 2014, with the fractional variability amplitude F_{var} increasing with frequency from the lowest 0.14 ± 0.01 for V-band flux to 0.45 ± 0.02 for X-ray flux, and then decreasing to 0.36 ± 0.06 for GeV gamma-ray flux, before increasing again to the highest value 0.54 ± 0.03 for TeV gamma-ray flux. Such a pattern in F_{var} is consistent with previous observations of gamma-ray blazars (see, e.g., Baloković et al. 2016, and references therein), with the highest F_{var} observed at the frequencies above the two peaks in the SED.

4.2. Cross-band Correlations

A moderate correlation between the TeV gamma-ray and X-ray fluxes from the source was observed. The best-fit power-law model suggests that the correlation is more than linear, with an index of 1.47 ± 0.13 , consistent with the expectation of a varying electron density and adiabatic cooling in an SSC model (Krawczynski et al. 2002; Katarzyński et al. 2005). The TeV gamma-ray and X-ray correlation could also give insights into whether the IC scattering occurs in the Thomson regime or KN regime, as the correlation may become closer to linear in the KN regime with the diminished scattering cross section (e.g., Aleksić et al. 2015; Baloković et al. 2016). More data are needed to quantify the correlation between X-rays and TeV gamma rays with a higher precision.

The correlation between the optical and TeV gamma-ray fluxes was weaker than that between X-ray and TeV gamma-ray fluxes, while the correlation between UV and TeV gamma-ray fluxes was comparable to that between the X-rays and TeV gamma rays, with a slightly higher correlation coefficient observed between the UVOT measurements with the UVW2 filter at the highest central frequency of $\sim 1.55 \times 10^{15}$ Hz. The UV/TeV gamma-ray correlation is more than quadratic, which could occur if the emitting region expands as the particle density increases (Katarzyński et al. 2005).

4.3. Upper Limits on the Redshift

Despite multiple measurement attempts (Shaw et al. 2013; Paiano et al. 2017), the redshift of VER J0521+211 remains uncertain. To facilitate the discussion, we adopt the value $z = 0.18$, the lower limit reported by Paiano et al. (2017). At this redshift, the luminosity distance is 878 Mpc (using $\Omega_m = 0.29$, $\Omega_\Lambda = 0.71$, and $H_0 = 69.6 \text{ km s}^{-1} \text{ Mpc}^{-1}$; Bennett et al. 2014), and the angular scale is roughly 3 pc mas^{-1} .

To help constrain the redshift of the source, upper limits were derived from the gamma-ray spectra using two methods based on Mazin & Goebel (2007) and Georganopoulos et al. (2010).

The first method (Mazin & Goebel 2007) assumes that the intrinsic gamma-ray spectrum follows a power law with an index of $\Gamma_{\text{int}} > 1.5$ (or more conservatively, $\Gamma_{\text{int}} > 0.7$). This method was used to derive the 95% upper limit on the redshift of $z < 0.34$ (and $z < 0.44$ for the conservative assumption of $\Gamma_{\text{int}} > 0.7$) for VER J0521+211 from VERITAS observations in 2009 and 2010 (Archambault et al. 2013). Using the same method, we find that the VERITAS spectrum on the night of the flare (BB2) offers a stronger constraint than other time periods, yielding a 95% upper limit on the redshift of $z < 0.38$ (and $z < 0.53$ for the conservative assumption of $\Gamma_{\text{int}} > 0.7$). We note that the deabsorbed VERITAS spectra at $z = 0.38$ are convex, with the measured fluxes at high energies significantly exceeding the best-fit power-law model, indicating that the redshift of the source is likely to be well below these limits.

The second method (Georganopoulos et al. 2010) assumes that the intrinsic TeV gamma-ray flux does not exceed the extrapolation of the GeV gamma-ray spectrum, which is minimally affected by the EBL for TeV blazars. A 95% upper limit on the optical depth from the EBL absorption can be calculated following Equation (2) in Aleksić et al. (2011):

$$\tau_{\gamma\gamma}(E) \leq \log \left[\frac{F_{\text{int}}(E)}{F_{\text{obs}} - 1.64 \Delta F_{\text{obs}}} \right],$$

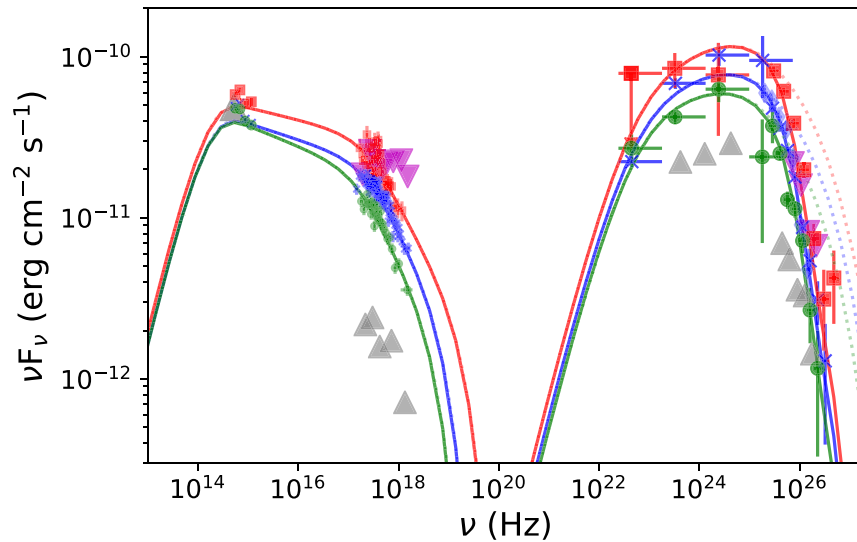


Figure 9. Broadband SED during the three Bayesian blocks obtained from the VERITAS light curve in the 2013–2014 season. The solid and dotted curves show the one-zone SSC model with the parameters listed in Table 4 with and without the EBL absorption (Franceschini et al. 2008). The blue crosses and filled diamonds, the red squares, and the green filled circles represent the first (BB1), second (BB2, flaring), and third (BB3) Bayesian blocks, respectively. Data are from Swift-UVOT, Swift-XRT, Fermi-LAT, MAGIC (only for BB1, shown as blue filled diamonds), and VERITAS, going from low to high frequencies. As a comparison, the magenta downward-pointing triangles and gray upward-pointing triangles show the flaring-state and low-state SEDs in 2009 from Archambault et al. (2013).

where $F_{\text{int}}(E)$ is the extrapolated GeV flux, representing the maximally allowed intrinsic flux, at energy E ; F_{obs} is the observed TeV gamma-ray flux; and ΔF_{obs} is the uncertainty of F_{obs} . The 95% upper limits on the optical depth $\tau_{\gamma\gamma}(E)$ derived from Fermi-LAT and VERITAS spectra for periods BB1, BB2, and BB3 are shown in the top panel of Figure 10. The spectrum from BB2 offers the strongest constraints on $\tau_{\gamma\gamma}(E)$. The optical depths $\tau_{\gamma\gamma}(z, E)$ for sources at a range of redshift of $0.25 \leq z \leq 0.35$ from four EBL models (Franceschini et al. 2008; Finke et al. 2010; Domínguez et al. 2011; Gilmore et al. 2012) were computed and compared to the constraints from VERITAS observations. The minimum difference between the observational constraints and the model-predicted optical depth, $\Delta\tau_{\gamma\gamma,\text{min}}(z, E)$, as a function of redshift is shown in the bottom panel of Figure 10. The 95% upper limits on the redshift of the source (corresponding to $\Delta\tau_{\gamma\gamma,\text{min}}(z, E) = 0$) were found to be $z \leq 0.3$, $z \leq 0.278$, $z \leq 0.308$, and $z \leq 0.281$ for the models from Domínguez et al. (2011), Finke et al. (2010), Franceschini et al. (2008), and Gilmore et al. (2012), respectively. These upper limits on the redshift are more constraining than the first method and those reported by Archambault et al. (2013). A precise measurement of the spectroscopic redshift of this source in the future will be important, as it helps constrain both the particle distribution and the EBL intensity.

4.4. An SSC Model for the Broadband SED

Three periods were identified with a Bayesian block analysis during which the source exhibited different TeV gamma-ray flux states (BB1, BB2, and BB3 as mentioned above). Broadband SEDs from UV to TeV gamma rays were constructed for each period. These SEDs are adequately described by a one-zone SSC model calculated following Krawczynski et al. (2002). The sets of parameters used to generate the SEDs shown in Figure 9 are listed in Table 4.

These parameters differ from those in the SSC model for the low-state SED from VERITAS data in 2009 (Archambault et al. 2013), where an even lower magnetic field strength of $B = 0.0025$ G results in a long synchrotron cooling time and a particle-dominated jet away from equipartition.

The simple SSC modeling provides several constraints on the properties of the source that are discussed below.

The peak frequency of the synchrotron radiation from the SSC model is roughly 5×10^{14} Hz, in the optical band and the IBL regime. However, as mentioned in Section 2.5, the synchrotron peak frequency closely depends on the intrinsic optical/UV spectrum and is heavily affected by extinction correction. If more substantial extinction from dust exists, the synchrotron peak would be in the UV band and the source in the HBL regime.

We note that it has been observed that the synchrotron peak frequency can shift between different flux states for blazars (e.g., Acciari et al. 2011; Valverde et al. 2020). Particularly, VER J0521+211 has been reported to exhibit HBL-like properties during a previous flare on 2009 November 27 (Archambault et al. 2013). The “flare” and “low-state” SEDs from Archambault et al. (2013) are shown, as a comparison to this work, as the magenta downward-pointing triangles and gray upward-pointing triangles in Figure 9. The TeV gamma-ray spectrum, including normalization and index, during the entire period studied in this work was comparable to that during the “flaring” state in 2009 November. However, while the X-ray spectra in this work were similar in normalization, they were much softer than those during the “flaring” state in 2009 November (with a photon index value of 2.0 ± 0.1 ; Archambault et al. 2013). This suggests strong synchrotron X-ray spectral variability on timescales of years for VER J0521+211. Moreover, the optical fluxes in this work were comparable to the low-state flux in Archambault et al. (2013), with a rather low variability amplitude. As the optical flux is only mildly affected by the extinction correction, this low variability amplitude in the optical band is robust.

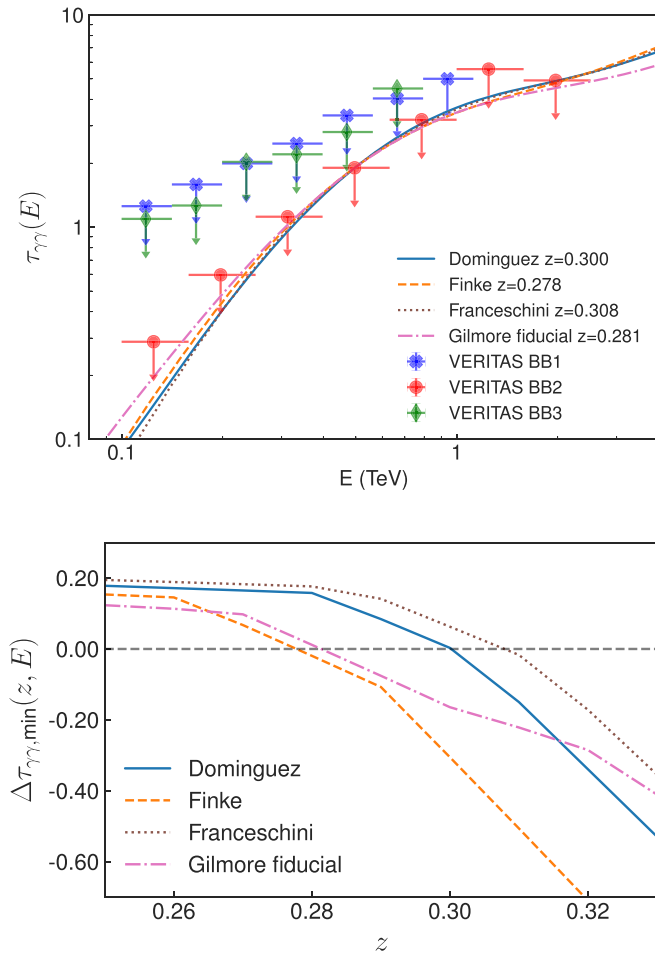


Figure 10. Top: the optical depth $\tau_{\gamma\gamma}(E)$ of the gamma rays due to $\gamma\gamma$ pair absorption induced by EBL photons. The blue filled crosses, the red filled circles, and the green filled diamonds show the 95% upper limits derived from VERITAS observations during periods BB1, BB2, and BB3, respectively. The optical depths $\tau_{\gamma\gamma}(z, E)$ from four EBL models, Domínguez et al. (2011; blue solid line), Finke et al. (2010; orange dashed line), Franceschini et al. (2008; copper dotted line), and Gilmore et al. (2012; pink dashed-dotted line), evaluated at the maximum redshift allowed by the 95% upper limits are also shown. Bottom: the minimum difference between the 95% upper limits on the EBL-induced pair absorption optical depth $\tau_{\gamma\gamma}(E)$ calculated from VERITAS data and the optical depth $\tau_{\gamma\gamma}(z, E)$ calculated from EBL models as a function of redshift.

The low optical variability implies that the SED at/below the synchrotron peak frequency does not change as much as that above the peak. The relatively flat spectrum from UV to X-ray bands indicates that the synchrotron peak is likely broad, making it difficult to measure the peak frequency and classify the blazar. On the other hand, the UV/X-ray spectrum of the source becomes harder with higher flux (as illustrated by the UV photon indices in Section 2.5 and the index-flux relation in Figure 6). The similar behavior of the observed UV and X-ray fluxes implies that the optical/UV bands are also likely located above the synchrotron SED peak, confirming the source as an IBL even in the higher flux state in 2013. The “harder-when-brighter” trend in both bands could be caused by the synchrotron SED peak shifting toward higher frequencies during flares. Such a behavior of the SED can be explained by changes to particles with the highest energies, e.g., from an evolving maximum or break particle energy or a change in the particle distribution shape above the break.

As the synchrotron peak frequency of VER J0521+211 is around the borderline between IBL and HBL, we review the radio features in the innermost jet region, which also provide insights into the blazar subclasses. Lister et al. (2019) identified six moving features in the inner jet from 15 GHz VLBA observations since 2009, including one that moves at a large apparent speed of $\sim 0.77 \pm 0.05 \text{ mas yr}^{-1}$ at $\sim 5 \text{ mas}$ from the core in mid-2014. On the other hand, three innermost features move at a very small apparent velocity, two of which even exhibited statistically significant inward motion. These slow features may be quasi-stationary. Such a combination of quasi-stationary and fast-moving radio knots is typically found in IBL/LBLs (e.g., Hervet et al. 2016). Therefore, the MOJAVE observations are consistent with the source being an IBL.

Interestingly, a 15 GHz moving feature at an apparent speed of $\sim 0.21 \pm 0.02 \text{ mas yr}^{-1}$ first appeared at around 5.5 mas ($\sim 11 \text{ pc}$) in 2012 December (Lister et al. 2018),⁸⁰ coincident with the period when the source exhibited elevated gamma-ray flux. Similar coincidences have been observed before in IBLs, but between fast gamma-ray flares on intraday timescales and moving knots at distances much closer to the core observed with the VLBA at 43 GHz (e.g., from BL Lacertae; Arlen et al. 2013; Abeysekara et al. 2018). The interactions between the moving and stationary radio features in the jet could provide a possible particle acceleration mechanism that leads to enhanced gamma-ray emission.

Based on the SSC model parameters (see Table 4), we can investigate the emission process of the particles at the source. The Lorentz factor of those electrons emitting the peak synchrotron radiation $\gamma_{\text{syn}} \approx 5.4 \times 10^4 (B/1 \text{ G})^{-1/2} [\delta/(1+z)]^{-1/2} (\nu_{\text{syn}}/10^{16} \text{ Hz})^{1/2} \approx 2 \times 10^4$ (for BB1/BB3), where B is the strength of the magnetic field, δ is the Doppler factor ($\delta = [\Gamma(1 - \beta \cos \theta)]^{-1} = 26$, where $\beta = (1 - 1/\Gamma^2)^{1/2}$), z is the redshift, and ν_{syn} is the peak frequency of the synchrotron radiation. The synchrotron cooling time of these electrons emitting at the peak frequency is $t_{\text{syn}} \approx 7.74 \times 10^8 \text{ s} \times (B/1 \text{ G})^{-2} \times \gamma^{-1} \approx 2000 \text{ days}$, corresponding to $\sim 78 \text{ days}$ in the observer’s frame. The electrons responsible for the peak synchrotron emission during BB2 have a slightly higher Lorentz factor of 2.1×10^4 and a cooling time of 73 days in the observer’s frame. As the synchrotron radiation energy density in the model is a few times larger than the magnetic field energy density, the cooling is likely dominated by the IC scattering, and the total observed cooling time can be as short as 2 weeks. Since the dynamic timescale is $R/c \sim 1.5 \text{ days}$ in the observers’ frame, the adiabatic cooling could also dominate the decay of the flux of the source.

Using the Lorentz factor of the electrons emitting at the synchrotron peak frequency γ_{syn} , we checked for the importance of the KN effects, which become substantial when the photon energy $h\nu^* > m_e c^2$ in the electron rest frame. Considering the IC scattering between the photons at the synchrotron peak frequency in the comoving frame $E'_{\text{peak}} \approx 0.1 \text{ eV}$ (primed quantities refer to those in the comoving frame) and the electrons that produce the peak synchrotron photons, we have $\gamma_{\text{syn}} E'_{\text{peak}} \approx 2 \text{ keV} < m_e c^2$. Therefore, the IC scattering of the peak of the synchrotron radiation field by electrons with γ_{syn} occurs in the Thomson regime (Acciari et al. 2011) and produces the observed IC

⁸⁰ http://www.physics.purdue.edu/astro/MOJAVE/sepvstime/0518+211_sepvstime.png

Table 4
Parameters Used for the One-zone SSC Models Shown in Figure 9

State	Γ	θ (deg)	B (10^{-2} G)	R (10^{17} cm)	w_e (10^{-3} erg cm^{-3})	$\log \frac{E_{\min}}{\text{eV}}$	$\log \frac{E_{\max}}{\text{eV}}$	$\log \frac{E_{\text{break}}}{\text{eV}}$	p_1	p_2
BB1	25	2.2	1.5	1.01	1.32	9.7	12.0	11.25	3.2	4.2
BB2	25	2.2	1.5	1.05	1.45	9.7	12.2	11.25	3.15	4.15
BB3	25	2.2	1.5	1.1	1.0	9.7	11.9	11.15	3.25	4.25
2009 ^a	30	...	0.25	4.0	...	10.25	12.0	...	3.0	...

Note. Γ and θ are the bulk Lorentz factor and the angle with respect to the line of sight of the relativistic emitting region, respectively; R is the radius of this region; B is the strength of the magnetic field; w_e is the energy density of the emitting electrons; $\log E_{\min}$, $\log E_{\max}$, and $\log E_{\text{break}}$ are the logarithms of the minimum, maximum, and break electron energies, respectively; p_1 and p_2 are the spectral indices of the electrons below and above the break energy, respectively. The corresponding parameters listed in Table 3 in Archambault et al. (2013) for the low-state SED in 2009 are also included for a comparison.

^a Archambault et al. (2013).

radiation up to $4\delta\gamma_{\text{syn}}^2 E'_{\text{peak}} \approx 4$ GeV, below the high-energy SED peak.

From the SED modeling, the SSC component peaks at a frequency $\nu_{\text{SSC}} \approx 4.4 \times 10^{24}$ Hz for the first two blocks and moves to a lower frequency $\nu_{\text{SSC}} \approx 2.6 \times 10^{24}$ Hz for the last, low-flux block. The shift of the SSC peak to higher frequencies during flares has been previously observed in blazars (e.g., Acciari et al. 2011). We also calculate the limit of the KN Doppler factor (Equation (17) in Tavecchio et al. 1998) $\delta < \delta_{\text{KN}} = [4\nu_{\text{syn}}\nu_{\text{SSC}}/(3(m_e c^2/h)^2)]^{1/2} \exp\{1/(\alpha_1 - 1) + 1/[2(\alpha_2 - \alpha_1)]\}^{-1/2}$, where the spectral indices below and above the IC peak are taken from Fermi-LAT and VERITAS observations as $\alpha_1 \approx 0.9$ and $\alpha_2 \approx 2.1$, respectively. In this case, the Doppler factor $\delta = 26$ is below the KN limit δ_{KN} ranging between about 40 and 60. As a result, the IC scattering that produces the peak SSC emission occurs in the KN regime. Note, however, that the observed SSC peak lies around 15 GeV; therefore, the best-fit index from the Fermi-LAT spectrum may not be a good estimator of α_1 . Moreover, the KN limit Doppler factor, defined as Equation (17) in Tavecchio et al. (1998), depends sensitively on α_1 . If we use a value of $\alpha_1 \approx 0.8$ as an example, the KN limit Doppler factor becomes about 6, placing the gamma-ray SED peak in the Thomson regime.

The maximum electron energy $E_{e,\text{max}}$ ranges between $10^{11.9}$ and $10^{12.2}$ eV (γ between about 1.6×10^6 and 3.1×10^6), and the observed maximum gamma-ray energy is $E_\gamma \sim 1$ TeV, corresponding to an energy of $E'_\gamma = E_\gamma(1+z)/\delta \sim 40$ GeV in the comoving frame. Therefore, we can estimate the energy range of the low-energy photons that participate in IC scattering and produce the observed gamma rays to be roughly between $E'_\gamma m_e^2 c^4 / E_{e,\text{max}}^2 \approx 0.01$ eV and $m_e^2 c^4 / E'_\gamma \sim 6.8$ eV in the comoving frame. These correspond to the observed photon energies between 0.25 and 175 eV, or between approximately 6×10^{13} Hz and 4×10^{16} Hz, ranging from the IR/optical bands up to the UV and soft X-ray band. In this scenario, we expect the observed emission at some of these lower energies to be strongly correlated with the gamma-ray emission. If the target photons of the observed energies above $\delta m_e c^2 / \gamma_{\text{max}} \sim 4$ eV were upscattered by the electrons at the maximum energy, the IC scattering would occur in the KN regime, leading to spectral breaks in the synchrotron spectrum that are not observed. However, the observed correlations between optical/UV and VHE fluxes (as shown in Figure 8) are not stronger than the observed X-ray/VHE correlation (as shown in Figure 7), implying that the lower-energy electrons and the target photons with observed energies above ~ 6.4 eV

(corresponding to the frequency of the UVW2 filter) are probably responsible for the observed VHE flux.

The electron break energy E_{brk} ranges between $10^{11.15}$ and $10^{11.25}$ eV (γ between 2.8×10^5 and 3.5×10^5). These electrons emit synchrotron radiation at around 2×10^{17} Hz (roughly 1 keV) and have a synchrotron cooling time of a few days in the observers' frame. Assuming that the mean free path (λ) of these electrons is comparable to their gyroradius of between 3.1×10^{10} cm and 3.9×10^{10} cm, we can estimate the electron diffusion coefficient $D \approx \lambda^2 / (2\lambda/c)$ to be a few times 10^{20} $\text{cm}^2 \text{s}^{-1}$. Taking the radius of the emitting region used in the SED modeling, we can estimate the escape timescale of the electrons at the break energy $\tau_{\text{esc}} \approx R^2 / (4D)$ to be on the order of 10^5 yr in the comoving frame, much longer than the cooling time.

The light-crossing time in the observer's frame is $2R'(1+z)/(cd) \sim 3$ days, shorter than the shortest Bayesian block interval (~ 5 days), and the model obeys causality.

A leptonic model has been used to describe the observed SED from VER J0521+211, allowing information about the jet environment to be inferred. It is possible that protons are accelerated in this same jet environment. By requiring protons to be magnetically confined within the emitting region (Hillas 1984), a rough estimation of the maximum proton energy can be calculated as $E_p < 3 \times 10^{-11}$ PeV $(B/1 \text{ G})(R/1 \text{ m}) \approx 500$ PeV. If photohadronic processes occur for protons at the maximum energy, the corresponding maximum energy of the produced neutrinos is then $E_\nu \leq \gamma_p m_\pi c^2 / 4 \approx 0.04 E_p \approx 20$ PeV (Rachen & Mészáros 1998), where γ_p is the Lorentz factor of the protons and m_π is the mass of a charged pion. Since no considerations were made of the acceleration, radiation, or escape processes of the protons, the maximum proton energy could be lower owing to the constraints from these processes. However, we do not rule out the possibility of neutrino production at energies up to 20 PeV in VER J0521+211 from the confinement argument alone. Given the relatively long duration of the elevated TeV gamma-ray flux, VER J0521+211 is potentially a good candidate for astrophysical neutrino searches.

5. Summary

The blazar VER J0521+211 was observed at an elevated gamma-ray state between 2013 and 2014 with VERITAS, MAGIC, and Fermi-LAT. The TeV gamma-ray flux above 200 GeV reached a peak of $(8.8 \pm 0.4) \times 10^{-7}$ photons $\text{m}^{-2} \text{s}^{-1}$ ($\sim 37\%$ of the Crab Nebula flux), and the monthly GeV gamma-ray flux above 100 MeV remained higher

than 7 times the 3FGL catalog value for a period that lasted 1 yr.

The fractional variability amplitude F_{var} was observed to be the lowest for the lowest-frequency V-band flux, increases with frequency to the X-ray band, and then decreases with frequency to the GeV energies, before increasing again to the highest at the highest TeV energies. Such a pattern of high variability amplitude F_{var} being observed at frequencies above the two peaks in the SED is consistent with previous observations of gamma-ray blazars (see, e.g., Baloković et al. 2016, and references therein).

A moderate more-than-linear correlation between the X-ray and TeV gamma-ray fluxes was observed, with a Pearson correlation coefficient of 0.7. The X-ray spectrum appeared harder when the flux was higher. Unlike the gamma-ray and X-ray bands, the optical flux did not increase significantly during the studied period compared to the archival low-state flux. The combination of low optical variability amplitude, higher X-ray variability amplitude, and “harder-when-brighter” trend in the X-ray spectrum indicates that the synchrotron peak of the SED may become broader during flaring states of this source, and the synchrotron peak frequency can shift to higher frequencies. Such a behavior of the SED can be explained by activity from particles with the highest energies. Of particular interest, the X-ray spectrum in 2013 and 2014 is much softer than that observed in a flaring state in 2009 (Archambault et al. 2013), while the normalization values are comparable, suggesting strong X-ray spectral variability on timescales of years.

The correlation between the optical and VHE fluxes is weaker than that between X-ray and VHE fluxes, while that between UV and VHE fluxes is the strongest and follows a more-than-quadratic relation, possibly from the combination of a varying particle density and an expansion of the emitting region (Katarzyński et al. 2005). The weaker correlation between the optical and VHE fluxes, as well as the low optical variability observed from 2009 to 2014, could also suggest that the optical emission from the source originates from a different region (see, e.g., Rajput et al. 2019).

Upper limits at the 95% confidence level on the redshift of the source were derived following Georganopoulos et al. (2010) and Aleksić et al. (2011) to be $z \leq 0.3$, $z \leq 0.278$, $z \leq 0.308$, and $z \leq 0.281$ using four EBL models from Domínguez et al. (2011), Finke et al. (2010), Franceschini et al. (2008), and Gilmore et al. (2012), respectively. These upper limits are more constraining than the previously reported value of $z < 0.34$ (Archambault et al. 2013). A precise redshift measurement of this source in the future will be important to studies of the particle distribution and the EBL intensity.

The broadband SED can be adequately described with a one-zone SSC model. The IC scattering in the source happens in the Thomson regime below the high-energy SED peak and likely transitions to the KN regime at or above the high-energy SED peak. In contrast to the hard X-ray spectrum and HBL-like SED properties of VER J0521+211 observed during the flaring state in 2009, the soft X-ray spectrum, the SED synchrotron peak frequency, the “harder-when-brighter” trend in both UV and X-ray bands, and the radio morphology from the MOJAVE program are all consistent with the source being an IBL object during the flaring state in 2013.

As a rare IBL that can be detected at TeV gamma-ray energies on timescales of months, more simultaneous MWL

observations of VER J0521+211 can provide valuable insights into this type of source. Of particular interest are the gamma-ray band and X-ray band, as they have exhibited more variability compared to other energies. Continued radio interferometry monitoring is also interesting for IBLs, as there could be a potential association between the ejection of superluminal knots and gamma-ray flares.

This research is supported by grants from the U.S. Department of Energy Office of Science, the U.S. National Science Foundation, and the Smithsonian Institution in the U.S.; by NSERC in Canada; and by the Helmholtz Association in Germany. This research used resources provided by the Open Science Grid, which is supported by the National Science Foundation and the U.S. Department of Energy’s Office of Science, and resources of the National Energy Research Scientific Computing Center (NERSC), a U.S. Department of Energy Office of Science User Facility operated under contract No. DE-AC02-05CH11231. We acknowledge the excellent work of the technical support staff at the Fred Lawrence Whipple Observatory and at the collaborating institutions in the construction and operation of the instrument.

The MAGIC Collaboration would like to thank the Instituto de Astrofísica de Canarias for the excellent working conditions at the Observatorio del Roque de los Muchachos in La Palma. The financial support of the German BMBF, MPG, and HGF; the Italian INFN and INAF; the Swiss National Fund SNF; the ERDF under the Spanish Ministerio de Ciencia e Innovación (MICINN) (PID2019-104114RB-C31, PID2019-104114RB-C32, PID2019-104114RB-C33, PID2019-105510GB-C31, PID2019-107847RB-C41, PID2019-107847RB-C42, PID2019-107847RB-C44, PID2019-107988GB-C22); the Indian Department of Atomic Energy; the Japanese ICRR, the University of Tokyo, JSPS, and MEXT; the Bulgarian Ministry of Education and Science, National RI Roadmap Project DOI-400/18.12.2020; and the Academy of Finland grant No. 320045 is gratefully acknowledged. This work was also supported by the Spanish Centro de Excelencia “Severo Ochoa” (SEV-2016-0588, SEV-2017-0709, CEX2019-000920-S), the Unidad de Excelencia “María de Maeztu” (CEX2019-000918-M, MDM-2015-0509-18-2), and the CERCA program of the Generalitat de Catalunya; by the Croatian Science Foundation (HrZZ) Project IP-2016-06-9782 and the University of Rijeka Project uniri-prirod-18-48; by the DFG Collaborative Research Centers SFB823/C4 and SFB876/C3; by the Polish National Research Centre grant UMO-2016/22/M/ST9/00382; and by the Brazilian National MCTIC, CNPq, and FAPERJ.

Q.F. was supported by NSF grant PHY-1806554 at Barnard College.

Facilities: VERITAS, MAGIC, Fermi(LAT), Swift(XRT), Steward Observatory, VLBA .

Software: Astropy (Astropy Collaboration et al. 2013, 2018), NumPy (van der Walt et al. 2011), Matplotlib (Hunter 2007), SciPy (Virtanen et al. 2020), seaborn (Waskom et al. 2014), HEASoft, VEGAS (Cogan 2008), Eventdisplay (Maier & Holder 2017), FermiTools.





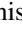

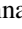

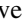
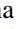


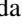
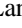

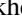
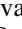

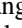


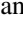
Appendix





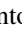

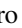








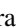



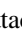
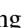

The X-ray spectral fit results using a log-parabola model for each observation are shown in Table 5.

Table 5
Results from X-Ray Spectral Analysis ($N_{\text{H}} = 4.38 \times 10^{21} \text{ cm}^{-2}$)

Observation	Start Time	Exposure (ks)	Energy Flux ($10^{-12} \text{ erg cm}^{-2} \text{ s}^{-1}$)	α	β	χ^2/dof
32628001	2012-11-13 09:46:51	2.0	$8.4^{+0.8}_{-0.9}$	3.00 ± 0.22	-0.37 ± 0.40	21.1/27
32628002	2012-11-14 08:14:59	2.3	$7.4^{+0.6}_{-0.4}$	3.65 ± 0.15	-0.74 ± 0.31	56.4/35
32628003	2012-11-15 08:17:59	1.8	$6.3^{+0.5}_{-0.9}$	3.83 ± 0.18	-1.21 ± 0.38	35.2/22
32628004	2012-11-16 08:34:59	1.9	$13.6^{+0.8}_{-1.0}$	3.19 ± 0.14	-0.46 ± 0.27	53.2/44
31531010	2013-10-15 09:22:59	1.5	$22.4^{+1.0}_{-1.2}$	2.10 ± 0.14	0.74 ± 0.24	40.9/42
31531011	2013-10-15 23:58:59	1.3	$20.3^{+1.1}_{-1.2}$	1.87 ± 0.18	1.08 ± 0.33	23.8/32
31531012	2013-10-17 14:13:59	1.6	$27.9^{+1.5}_{-1.8}$	1.98 ± 0.14	0.70 ± 0.23	55.1/44
31531013	2013-10-18 11:29:59	0.7	$36.8^{+1.9}_{-2.3}$	1.80 ± 0.18	0.82 ± 0.29	23.4/31
31531014	2013-10-19 17:31:17	1.4	$18.3^{+1.0}_{-1.0}$	2.31 ± 0.15	0.56 ± 0.27	29.9/33
31531015	2013-10-20 11:05:59	1.6	$24.0^{+1.3}_{-1.3}$	2.13 ± 0.15	0.26 ± 0.25	42.1/38
31531016	2013-10-21 00:01:58	1.4	$31.0^{+1.4}_{-1.4}$	2.11 ± 0.12	0.47 ± 0.20	66.4/53
31531017	2013-10-25 18:04:59	1.3	$30.4^{+1.5}_{-1.1}$	2.06 ± 0.14	0.64 ± 0.24	63.5/48
31531018	2013-10-26 10:06:29	0.1	$25.3^{+7.5}_{-45.3}$	2.51 ± 0.62	-0.16 ± 1.75	0.0/1
31531019	2013-10-27 05:14:59	1.4	$22.1^{+1.6}_{-1.8}$	1.87 ± 0.23	0.74 ± 0.39	17.4/21
31531020	2013-11-25 05:28:59	2.1	$11.7^{+0.7}_{-1.1}$	1.63 ± 0.29	1.73 ± 0.51	35.6/18
31531021	2013-11-26 05:30:59	2.1	$19.9^{+0.6}_{-1.0}$	2.25 ± 0.12	0.84 ± 0.22	69.4/55
31531022	2013-11-27 07:07:59	2.0	$14.1^{+0.6}_{-1.1}$	2.27 ± 0.16	0.77 ± 0.33	20.9/32
31531023	2013-11-28 07:09:59	2.1	$13.1^{+0.7}_{-0.5}$	2.31 ± 0.16	0.75 ± 0.30	20.5/30
31531024	2013-11-29 07:11:59	2.0	$17.6^{+0.7}_{-0.9}$	2.18 ± 0.14	0.57 ± 0.27	40.1/42
31531025	2013-11-30 07:12:59	1.7	$23.5^{+0.9}_{-1.3}$	2.13 ± 0.13	0.82 ± 0.23	43.5/46
31531026	2013-12-01 08:50:59	1.9	$13.0^{+1.1}_{-1.1}$	2.49 ± 0.16	0.05 ± 0.31	32.7/27
31531027	2013-12-02 07:15:59	2.0	$15.1^{+1.1}_{-0.6}$	1.90 ± 0.18	1.04 ± 0.31	38.6/36
31531028	2013-12-03 07:17:59	1.9	$28.9^{+1.9}_{-1.1}$	2.28 ± 0.12	0.51 ± 0.25	21.2/12
32628005	2013-12-24 04:37:59	1.5	$9.5^{+0.7}_{-1.0}$	2.26 ± 0.23	0.49 ± 0.43	6.7/16
32628006	2013-12-25 04:32:59	1.5	$11.9^{+0.7}_{-1.0}$	2.00 ± 0.20	1.11 ± 0.39	19.7/24
32628007	2013-12-26 04:38:59	1.4	$15.9^{+0.9}_{-1.3}$	2.08 ± 0.19	0.73 ± 0.32	31.4/27
32628009	2013-12-28 04:35:59	1.5	$16.0^{+0.6}_{-1.0}$	2.09 ± 0.16	0.93 ± 0.27	24.1/33
32628010	2013-12-29 04:48:59	1.4	$6.8^{+0.6}_{-1.0}$	2.42 ± 0.27	0.76 ± 0.62	10.7/11
32628011	2013-12-30 04:32:59	1.4	$8.4^{+0.5}_{-0.6}$	2.34 ± 0.22	1.20 ± 0.47	17.8/17
32628012	2013-12-31 04:36:59	1.5	$7.2^{+0.5}_{-0.6}$	2.53 ± 0.22	0.95 ± 0.48	15.2/15
32628013	2014-01-01 04:36:59	1.5	$18.4^{+1.0}_{-1.1}$	2.20 ± 0.15	0.60 ± 0.26	26.8/35
32628014	2014-01-16 14:27:59	0.9	$18.4^{+2.0}_{-1.6}$	1.81 ± 0.24	0.92 ± 0.44	12.7/18

ORCID iDs

W. Benbow  <https://orcid.org/0000-0003-2098-170X>
A. Brill  <https://orcid.org/0000-0002-6208-5244>
Q. Feng  <https://orcid.org/0000-0001-6674-4238>
L. Fortson  <https://orcid.org/0000-0002-1067-8558>
A. Furniss  <https://orcid.org/0000-0003-1614-1273>
A. Gent  <https://orcid.org/0000-0001-7429-3828>
D. Hanna  <https://orcid.org/0000-0002-8513-5603>
T. Hassan  <https://orcid.org/0000-0002-4758-9196>
O. Hervet  <https://orcid.org/0000-0003-3878-1677>
B. Hona  <https://orcid.org/0000-0002-7609-343X>
W. Jin  <https://orcid.org/0000-0002-1089-1754>
P. Kaaret  <https://orcid.org/0000-0002-3638-0637>
D. Kieda  <https://orcid.org/0000-0003-4785-0101>
M. J. Lang  <https://orcid.org/0000-0003-4641-4201>
G. Maier  <https://orcid.org/0000-0001-9868-4700>
R. Mukherjee  <https://orcid.org/0000-0002-3223-0754>
M. Nievas-Rosillo  <https://orcid.org/0000-0002-8321-9168>
R. A. Ong  <https://orcid.org/0000-0002-4837-5253>
K. Pfrang  <https://orcid.org/0000-0002-7990-7179>
M. Pohl  <https://orcid.org/0000-0001-7861-1707>
E. Pueschel  <https://orcid.org/0000-0002-0529-1973>
K. Ragan  <https://orcid.org/0000-0002-5351-3323>

D. Ribeiro  <https://orcid.org/0000-0002-7523-7366>
I. Sadeh  <https://orcid.org/0000-0003-1387-8915>
V. A. Acciari  <https://orcid.org/0000-0001-8307-2007>
S. Ansoldi  <https://orcid.org/0000-0002-5613-7693>
L. A. Antonelli  <https://orcid.org/0000-0002-5037-9034>
A. Arbet Engels  <https://orcid.org/0000-0001-9076-9582>
M. Artero  <https://orcid.org/0000-0002-4899-8127>
K. Asano  <https://orcid.org/0000-0001-9064-160X>
D. Baack  <https://orcid.org/0000-0002-2311-4460>
A. Babić  <https://orcid.org/0000-0002-1444-5604>
A. Baquero  <https://orcid.org/0000-0002-1757-5826>
U. Barres de Almeida  <https://orcid.org/0000-0001-7909-588X>
J. A. Barrio  <https://orcid.org/0000-0002-0965-0259>
I. Batković  <https://orcid.org/0000-0002-1209-2542>
J. Becerra González  <https://orcid.org/0000-0002-6729-9022>
W. Bednarek  <https://orcid.org/0000-0003-0605-108X>
E. Bernardini  <https://orcid.org/0000-0003-3108-1141>
A. Berti  <https://orcid.org/0000-0003-0396-4190>
W. Bhattacharyya  <https://orcid.org/0000-0003-4751-0414>
C. Bigongiari  <https://orcid.org/0000-0003-3293-8522>
A. Biland  <https://orcid.org/0000-0002-1288-833X>
O. Blanch  <https://orcid.org/0000-0002-8380-1633>

- H. Bökenkamp <https://orcid.org/0000-0001-5787-3687>
 G. Bonnoli <https://orcid.org/0000-0003-2464-9077>
 Ž. Bošnjak <https://orcid.org/0000-0001-6536-0320>
 G. Busetto <https://orcid.org/0000-0002-2687-6380>
 R. Carosi <https://orcid.org/0000-0002-4137-4370>
 G. Ceribella <https://orcid.org/0000-0002-9768-2751>
 M. Cerruti <https://orcid.org/0000-0001-7891-699X>
 Y. Chai <https://orcid.org/0000-0003-2816-2821>
 A. Chilingarian <https://orcid.org/0000-0002-2018-9715>
 E. Colombo <https://orcid.org/0000-0002-3700-3745>
 J. L. Contreras <https://orcid.org/0000-0001-7282-2394>
 J. Cortina <https://orcid.org/0000-0003-4576-0452>
 S. Covino <https://orcid.org/0000-0001-9078-5507>
 G. D'Amico <https://orcid.org/0000-0001-6472-8381>
 V. D'Elia <https://orcid.org/0000-0002-7320-5862>
 P. Da Vela <https://orcid.org/0000-0003-0604-4517>
 F. Dazzi <https://orcid.org/0000-0001-5409-6544>
 A. De Angelis <https://orcid.org/0000-0002-3288-2517>
 B. De Lotto <https://orcid.org/0000-0003-3624-4480>
 A. Del Popolo <https://orcid.org/0000-0002-9057-0239>
 M. Delfino <https://orcid.org/0000-0002-9468-4751>
 J. Delgado <https://orcid.org/0000-0002-0166-5464>
 C. Delgado Mendez <https://orcid.org/0000-0002-7014-4101>
 D. Depaoli <https://orcid.org/0000-0002-2672-4141>
 F. Di Piero <https://orcid.org/0000-0003-4861-432X>
 L. Di Venere <https://orcid.org/0000-0003-0703-824X>
 E. Do Souto Espiñeira <https://orcid.org/0000-0001-6974-2676>
 D. Dominis Prester <https://orcid.org/0000-0002-9880-5039>
 A. Donini <https://orcid.org/0000-0002-3066-724X>
 D. Dorner <https://orcid.org/0000-0001-8823-479X>
 M. Doro <https://orcid.org/0000-0001-9104-3214>
 D. Elsaesser <https://orcid.org/0000-0001-6796-3205>
 V. Fallah Ramazani <https://orcid.org/0000-0001-8991-7744>
 L. Fariña <https://orcid.org/0000-0003-4116-6157>
 A. Fattorini <https://orcid.org/0000-0002-1056-9167>
 L. Font <https://orcid.org/0000-0003-2109-5961>
 C. Fruck <https://orcid.org/0000-0001-5880-7518>
 S. Fukami <https://orcid.org/0000-0003-4025-7794>
 Y. Fukazawa <https://orcid.org/0000-0002-0921-8837>
 R. J. García López <https://orcid.org/0000-0002-2144-0991>
 M. Garczarczyk <https://orcid.org/0000-0002-0445-4566>
 M. Gaug <https://orcid.org/0000-0001-8442-7877>
 N. Giglietto <https://orcid.org/0000-0002-9021-2888>
 F. Giordano <https://orcid.org/0000-0002-8651-2394>
 P. Gliwny <https://orcid.org/0000-0002-4183-391X>
 N. Godinović <https://orcid.org/0000-0002-4674-9450>
 J. G. Green <https://orcid.org/0000-0002-1130-6692>
 D. Green <https://orcid.org/0000-0003-0768-2203>
 D. Hadasch <https://orcid.org/0000-0001-8663-6461>
 A. Hahn <https://orcid.org/0000-0003-0827-5642>
 T. Hassan <https://orcid.org/0000-0002-4758-9196>
 L. Heckmann <https://orcid.org/0000-0002-6653-8407>
 J. Herrera <https://orcid.org/0000-0002-3771-4918>
 D. Hrupec <https://orcid.org/0000-0002-7027-5021>
 M. Hütten <https://orcid.org/0000-0002-2133-5251>
 T. Inada <https://orcid.org/0000-0002-6923-9314>
 K. Ishio <https://orcid.org/0000-0003-3189-0766>
 I. Jiménez Martínez <https://orcid.org/0000-0003-2150-6919>
 L. Jouvin <https://orcid.org/0000-0001-5119-8537>
 D. Kerszberg <https://orcid.org/0000-0002-5289-1509>
 Y. Kobayashi <https://orcid.org/0000-0001-5551-2845>
 H. Kubo <https://orcid.org/0000-0001-9159-9853>
 J. Kushida <https://orcid.org/0000-0002-8002-8585>
 A. Lamastra <https://orcid.org/0000-0003-2403-913X>
 D. Lelas <https://orcid.org/0000-0002-8269-5760>
 F. Leone <https://orcid.org/0000-0001-7626-3788>
 E. Lindfors <https://orcid.org/0000-0002-9155-6199>
 L. Linhoff <https://orcid.org/0000-0001-6330-7286>
 S. Lombardi <https://orcid.org/0000-0002-6336-865X>
 F. Longo <https://orcid.org/0000-0003-2501-2270>
 R. López-Coto <https://orcid.org/0000-0002-3882-9477>
 M. López-Moya <https://orcid.org/0000-0002-8791-7908>
 A. López-Oramas <https://orcid.org/0000-0003-4603-1884>
 S. Loporchio <https://orcid.org/0000-0003-4457-5431>
 B. Machado de Oliveira Fraga <https://orcid.org/0000-0002-6395-3410>
 C. Maggio <https://orcid.org/0000-0003-0670-7771>
 P. Majumdar <https://orcid.org/0000-0002-5481-5040>
 M. Makariev <https://orcid.org/0000-0002-1622-3116>
 G. Maneva <https://orcid.org/0000-0002-5959-4179>
 M. Manganaro <https://orcid.org/0000-0003-1530-3031>
 K. Mannheim <https://orcid.org/0000-0002-2950-6641>
 M. Mariotti <https://orcid.org/0000-0003-3297-4128>
 M. Martínez <https://orcid.org/0000-0002-9763-9155>
 A. Mas Aguilar <https://orcid.org/0000-0002-8893-9009>
 D. Mazin <https://orcid.org/0000-0002-2010-4005>
 S. Mender <https://orcid.org/0000-0002-0755-0609>
 S. Mićanović <https://orcid.org/0000-0002-0076-3134>
 D. Miceli <https://orcid.org/0000-0002-2686-0098>
 T. Miener <https://orcid.org/0000-0003-1821-7964>
 J. M. Miranda <https://orcid.org/0000-0002-1472-9690>
 R. Mirzoyan <https://orcid.org/0000-0003-0163-7233>
 E. Molina <https://orcid.org/0000-0003-1204-5516>
 A. Moralejo <https://orcid.org/0000-0002-1344-9080>
 D. Morcuende <https://orcid.org/0000-0001-9400-0922>
 V. Moreno <https://orcid.org/0000-0002-8358-2098>
 T. Nakamori <https://orcid.org/0000-0002-7308-2356>
 L. Nava <https://orcid.org/0000-0001-5960-0455>
 V. Neustroev <https://orcid.org/0000-0003-4772-595X>
 M. Nievas Rosillo <https://orcid.org/0000-0002-8321-9168>
 C. Nigro <https://orcid.org/0000-0001-8375-1907>
 K. Nilsson <https://orcid.org/0000-0002-1445-8683>
 K. Nishijima <https://orcid.org/0000-0002-1830-4251>
 K. Noda <https://orcid.org/0000-0003-1397-6478>
 S. Nozaki <https://orcid.org/0000-0002-6246-2767>
 Y. Ohtani <https://orcid.org/0000-0001-7042-4958>
 T. Oka <https://orcid.org/0000-0002-9924-9978>
 J. Otero-Santos <https://orcid.org/0000-0002-4241-5875>
 S. Paiano <https://orcid.org/0000-0002-2239-3373>
 M. Palatiello <https://orcid.org/0000-0002-4124-5747>
 D. Paneque <https://orcid.org/0000-0002-2830-0502>
 R. Paoletti <https://orcid.org/0000-0003-0158-2826>
 J. M. Paredes <https://orcid.org/0000-0002-1566-9044>
 L. Pavletić <https://orcid.org/0000-0002-9926-0405>
 P. Peñil <https://orcid.org/0000-0003-3741-9764>
 M. Persic <https://orcid.org/0000-0003-1853-4900>
 P. G. Prada Moroni <https://orcid.org/0000-0001-9712-9916>
 E. Prandini <https://orcid.org/0000-0003-4502-9053>
 C. Priyadarshi <https://orcid.org/0000-0002-9160-9617>
 I. Puljak <https://orcid.org/0000-0001-7387-3812>
 W. Rhode <https://orcid.org/0000-0003-2636-5000>
 M. Ribó <https://orcid.org/0000-0002-9931-4557>
 J. Rico <https://orcid.org/0000-0003-4137-1134>

C. Righi <https://orcid.org/0000-0002-1218-9555>
 A. Rugliancich <https://orcid.org/0000-0001-5471-4701>
 N. Sahakyan <https://orcid.org/0000-0003-2011-2731>
 T. Saito <https://orcid.org/0000-0001-6201-3761>
 S. Sakurai <https://orcid.org/0000-0001-7427-4520>
 K. Satalecka <https://orcid.org/0000-0002-7669-266X>
 F. G. Saturni <https://orcid.org/0000-0002-1946-7706>
 B. Schleicher <https://orcid.org/0000-0001-8624-8629>
 K. Schmidt <https://orcid.org/0000-0002-9883-4454>
 J. Sitarek <https://orcid.org/0000-0002-1659-5374>
 D. Sobczynska <https://orcid.org/0000-0003-4973-7903>
 A. Spolon <https://orcid.org/0000-0001-8770-9503>
 A. Stamerra <https://orcid.org/0000-0002-9430-5264>
 J. Striškoivić <https://orcid.org/0000-0003-2902-5044>
 D. Strom <https://orcid.org/0000-0003-2108-3311>
 M. Strzys <https://orcid.org/0000-0001-5049-1045>
 Y. Suda <https://orcid.org/0000-0002-2692-5891>
 M. Takahashi <https://orcid.org/0000-0002-0574-6018>
 R. Takeishi <https://orcid.org/0000-0001-6335-5317>
 F. Tavecchio <https://orcid.org/0000-0003-0256-0995>
 P. Temnikov <https://orcid.org/0000-0002-9559-3384>
 T. Terzić <https://orcid.org/0000-0002-4209-3407>
 A. Tutone <https://orcid.org/0000-0002-2840-0001>
 J. van Scherpenberg <https://orcid.org/0000-0002-6173-867X>
 G. Vanzo <https://orcid.org/0000-0003-1539-3268>
 M. Vazquez Acosta <https://orcid.org/0000-0002-2409-9792>
 S. Ventura <https://orcid.org/0000-0001-7065-5342>
 V. Verguillov <https://orcid.org/0000-0001-7911-1093>
 I. Viale <https://orcid.org/0000-0001-5031-5930>
 C. F. Vigorito <https://orcid.org/0000-0002-0069-9195>
 V. Vitale <https://orcid.org/0000-0001-8040-7852>
 I. Vovk <https://orcid.org/0000-0003-3444-3830>
 M. Will <https://orcid.org/0000-0002-7504-2083>
 C. Wunderlich <https://orcid.org/0000-0002-9604-7836>
 T. Yamamoto <https://orcid.org/0000-0001-9734-8203>
 D. Zarić <https://orcid.org/0000-0001-5763-9487>

References

Abdo, A. A., Ackermann, M., Ajello, M., et al. 2010, *Natur*, 463, 919
 Abeyssekara, A. U., Benbow, W., Bird, R., et al. 2018, *ApJ*, 856, 95
 Acciari, V. A., Arlen, T., Aune, T., et al. 2011, *ApJ*, 729, 2
 Acero, F., Ackermann, M., Ajello, M., et al. 2015, *ApJS*, 218, 23
 Aleksić, J., Ansoldi, S., Antonelli, L. A., et al. 2015, *A&A*, 578, A22
 Aleksić, J., Ansoldi, S., Antonelli, L. A., et al. 2016, *Aph*, 72, 76
 Aleksić, J., Antonelli, L. A., Antoranz, P., et al. 2011, *ApJL*, 730, L8
 Archambault, S., Arlen, T., Aune, T., et al. 2013, *ApJ*, 776, 69
 Archambault, S., Aune, T., Behera, B., et al. 2014, *ApJL*, 785, L16
 Arlen, T., Aune, T., Beilicke, M., et al. 2013, *ApJ*, 762, 92
 Astropy Collaboration, Price-Whelan, A. M., Sipőcz, B. M., et al. 2018, *AJ*, 156, 123
 Astropy Collaboration, Robitaille, T. P., Tollerud, E. J., et al. 2013, *A&A*, 558, A33

Atwood, W., Albert, A., Baldini, L., et al. 2013, arXiv:1303.3514
 Atwood, W. B., Abdo, A. A., Ackermann, M., et al. 2009, *ApJ*, 697, 1071
 Baloković, M., Paneque, D., Madejski, G., et al. 2016, *ApJ*, 819, 156
 Bennett, C. L., Larson, D., Weiland, J. L., & Hinshaw, G. 2014, *ApJ*, 794, 135
 Burrows, D. N., Hill, J. E., Nousek, J. A., et al. 2005, *SSRv*, 120, 165
 Buson, S. 2013, *ATel*, 5472, 1
 Cogan, P. 2008, in Proc. of the 30th Int. Cosmic Ray Conf., ed. R. Caballero et al. (New York: AIP), 1385
 Domínguez, A., Primack, J. R., Rosario, D. J., et al. 2011, *MNRAS*, 410, 2556
 Finke, J. D., Razzaque, S., & Dermer, C. D. 2010, *ApJ*, 712, 238
 Fossati, G., Maraschi, L., Celotti, A., Comastri, A., & Ghisellini, G. 1998, *MNRAS*, 299, 433
 Franceschini, A., Rodighiero, G., & Vaccari, M. 2008, *A&A*, 487, 837
 Gehrels, N., Chincarini, G., Giommi, P., et al. 2004, *ApJ*, 611, 1005
 Georganopoulos, M., Finke, J. D., & Reyes, L. C. 2010, *ApJ*, 714, L157
 Gilmore, R. C., Somerville, R. S., Primack, J. R., & Domínguez, A. 2012, *MNRAS*, 422, 3189
 Hervet, O., Boisson, C., & Sol, H. 2016, *A&A*, 592, A22
 Hillas, A. M. 1984, *ARA&A*, 22, 425
 Hunter, J. D. 2007, *CSE*, 9, 90
 Kalberla, P. M. W., Burton, W. B., Hartmann, D., et al. 2005, *A&A*, 440, 775
 Katarzyński, K., Ghisellini, G., Tavecchio, F., et al. 2005, *A&A*, 433, 479
 Kharb, P., Lister, M. L., & Shastri, P. 2008, *IJMPD*, 17, 1545
 Komisarov, S. S., & Falle, S. A. E. G. 1998, *MNRAS*, 297, 1087
 Krawczynski, H., Coppi, P. S., & Aharonian, F. 2002, *MNRAS*, 336, 721
 Lister, M. L., Aller, M. F., Aller, H. D., et al. 2018, *ApJS*, 234, 12
 Lister, M. L., Homan, D. C., Hovatta, T., et al. 2019, *ApJ*, 874, 43
 MAGIC Collaboration, Acciari, V. A., Ansoldi, S., et al. 2019, *A&A*, 623, A175
 MAGIC Collaboration, Ahnen, M. L., Ansoldi, S., et al. 2018, *A&A*, 619, A45
 Maier, G., & Holder, J. 2017, in Proc. of the 35th Int. Cosmic Ray Conf. (ICRC2017) (New York: AIP)
 Mazin, D., & Goebel, F. 2007, *ApJ*, 655, L13
 Moretti, A., Campana, S., Mineo, T., et al. 2005, *Proc. SPIE*, 5898, 360
 Narayan, R., Li, J., & Tchekhovskoy, A. 2009, *ApJ*, 697, 1681
 Paiano, S., Landoni, M., Falomo, R., et al. 2017, *ApJ*, 837, 144
 Park, N. & The VERITAS Collaboration 2015, in Proc. of the 34th Int. Cosmic Ray Conf. (ICRC2015) (New York: AIP)
 Poole, T. S., Breeveld, A. A., Page, M. J., et al. 2008, *MNRAS*, 383, 627
 Poutanen, J., Zdziarski, A. A., & Ibragimov, A. 2008, *MNRAS*, 389, 1427
 Rachen, J. P., & Mészáros, P. 1998, *PhRvD*, 58, 123005
 Rajput, B., Stalin, C. S., Sahayanathan, S., Rakshit, S., & Mandal, A. K. 2019, *MNRAS*, 486, 1781
 Roming, P. W. A., Kennedy, T. E., Mason, K. O., et al. 2005, *SSRv*, 120, 95
 Roming, P. W. A., Koch, T. S., Oates, S. R., et al. 2009, *ApJ*, 690, 163
 Scargle, J. D., Norris, J. P., Jackson, B., & Chiang, J. 2013, *ApJ*, 764, 167
 Schlafly, E. F., & Finkbeiner, D. P. 2011, *ApJ*, 737, 103
 Schlegel, D. J., Finkbeiner, D. P., & Davis, M. 1998, *ApJ*, 500, 525
 Shaw, M. S., Romani, R. W., Cotter, G., et al. 2013, *ApJ*, 764, 135
 Smith, P. S., Montiel, E., Rightley, S., et al. 2009, arXiv:0912.3621
 Tavecchio, F., Maraschi, L., & Ghisellini, G. 1998, *ApJ*, 509, 608
 Urry, C. M., & Padovani, P. 1995, *PASP*, 107, 803
 Valverde, J., Horan, D., Bernard, D., et al. 2020, *ApJ*, 891, 170
 van der Walt, S., Colbert, S. C., & Varoquaux, G. 2011, *CSE*, 13, 22
 Vaughan, S., Edelson, R., Warwick, R. S., & Uttley, P. 2003, *MNRAS*, 345, 1271
 Virtanen, P., Gommers, R., Oliphant, T. E., et al. 2020, *NatMe*, 17, 261
 Waskom, M., Botvinnik, O., Hobson, P., et al. 2014, *JOSS*, 6, 3021
 Willingale, R., Starling, R. L. C., Beardmore, A. P., Tanvir, N. R., & O'Brien, P. T. 2013, *MNRAS*, 431, 394